

Chapter 5

The Mesoscopic Nature of Quantum Dots in Photon Emission

P. Tighineanu, A.S. Sørensen, S. Stobbe and P. Lodahl

Abstract Semiconductor quantum dots share many properties with atoms such as discrete spectrum, which implies the ability to emit high purity single photons. However, they have unique features as well that are unknown to other emitters: they embody tens of thousands of atoms attaining large mesoscopic sizes, and lack the common atomic symmetries. Here we discuss two effects that are mediated by the mesoscopic nature and render quantum dots fundamentally different than atoms. The mesoscopic size and lack of parity symmetry causes the electric-dipole approximation to not be applicable to In(Ga)As quantum dots. As a consequence, the latter do not fulfil the atomic selection rules and thus interact with the electric and magnetic components of light on the same electronic transition. The multi-atomic nature also causes a collective mesoscopic effect in monolayer-fluctuation GaAs quantum dots, namely single-photon superradiance, giving rise to a giant light-matter coupling strength.

Semiconductor quantum dots (QDs) provide the essential link between light and matter and can be integrated monolithically into photonic devices. These nanometer-sized purposefully engineered impurities combine the atomic-like discrete spectra and excellent single-photon purity with the large light-matter interaction strength inherent to solid-state systems [1]. The ability to tailor the photonic environment around QDs has resulted in tremendous progress in manipulating single QD excitations. Strong coupling between a QD and a cavity [2–4] and near-unity coupling to a photonic waveguide [5–10] are a few out of many exciting realizations [1].

The atomic-like properties of QDs are supplemented by a range of new effects owing to their solid-state nature. For instance, vibrations of the underlying crystal lattice, known as phonons, may decohere the light-matter interaction [11–13] or couple non-resonant QD excitations to an optical cavity [14–18]. Similarly, the mesoscopic

P. Tighineanu (✉) · A.S. Sørensen · S. Stobbe · P. Lodahl
The Niels Bohr Institute, University of Copenhagen, Blegdamsvej 17,
2100 Copenhagen, Denmark
e-mail: petrut@nbi.ku.dk

P. Lodahl
e-mail: lodahl@nbi.ku.dk

ensemble of the nuclei composing the QD can be used to tailor the hyperfine interaction with the electron in spin-based quantum-information science [19]. Recently it was found [20] that QDs may break the dipole approximation, which is often assumed to be valid also in solid-state quantum optics. These realizations unveil the complex nature of QDs, which embody tens to hundred thousand atoms attaining “mesoscopic” sizes that interact relentlessly with the surrounding solid-state environment. In this chapter we present a unified description of the mesoscopic nature of QDs [20–23]. In particular, we discuss two mesoscopic effects that exist solely due to the large physical size of QDs: the breakdown of the dipole theory of In(Ga)As QDs and collective enhancement of light-matter interaction with monolayer-fluctuation GaAs QDs.

The small size L of most quantum emitters compared to the wavelength of light λ has ensured the success of the dipole theory, which states that emitters interact with light as dimensionless entities (point dipoles). Since QDs attain mesoscopic sizes of 10–30 nm [24], the dipole approximation does not necessarily hold because the figure of merit $2\pi nL/\lambda_0 \approx 0.5$ is not negligible. Here, typical values for the wavelength in vacuum $\lambda_0 = 900$ nm, refractive index $n = 3.42$ and $L = 20$ nm have been used. This figure of merit may be further enhanced in the vicinity of metal nanostructures, where additional propagating modes (surface plasmons) beyond the light cone arise. It has been observed that the spontaneous-emission dynamics from QDs placed near a metal interface show pronounced deviations from the dipole theory [20]. A theory of light-matter interaction beyond the dipole theory can explain these experimental findings by introducing a single mesoscopic moment to be considered along with the dipole moment in light-matter interactions [21]. Notably, this theory is more general than previously developed models [25–32] because it considers the symmetry of the full quantum-mechanical wavefunction and not only the slowly varying envelope. We show that the discrete atomistic symmetry explains the microscopic origin of the large mesoscopic moment observed experimentally. In particular, the developed theory pinpoints that large structural inhomogeneities at the crystal-lattice level lead to a violation of parity symmetry in In(Ga)As QDs [22]. Quantum dots therefore break the atomic selection rules and probe electric and magnetic fields on the same electronic transition [21]. Moreover, the mesoscopic size of QDs may ease the observation of dipole-forbidden transitions in photonic nanostructures [33]. It has been shown that, in the opposite limit of highest possible (spherical) symmetry present in, e.g., colloidal QDs, a shell theorem is valid, which states that the Purcell enhancement in an arbitrary photonic environment is protected by symmetry and does not depend on the QD size [32].

The second part of this chapter is devoted to presenting another mesoscopic property of QDs, namely collective enhancement of light-matter interaction leading to single-photon superradiance. Quantum dots benefit from their multi-body nature with an enhanced coupling to light compared to atoms, which renders them promising candidates for improving the efficiency of single-photon sources, solar cells and nano-lasers, to name a few important practical applications. Commonly employed QDs have, however, an upper limit for the interaction strength with light, regardless of their size and shape. It has therefore been a long-sought goal in quantum photonics

to develop solid-state emitters beyond this upper limit [34–37]. We demonstrate that the fundamental excitation of a monolayer-fluctuation QD [38] is analogous to the phenomenon of single-photon superradiance defined by Dicke for a non-interacting ensemble [39]. This effect leads to an enhanced coupling to light far beyond that of conventional QDs, which may be of interest for fundamental science and technology alike. In particular, such rapid radiative decays will likely exceed relevant dephasing mechanisms resulting in highly coherent flying quantum bits. Furthermore, new and so far largely unexplored solid-state quantum-electrodynamics regimes involving energy non-conserving virtual processes, such as the ultra-strong coupling between light and matter, may become within reach at optical frequencies [23].

5.1 Fundamentals of Light-Matter Interaction with Quantum Dots

In this section we lay the fundamental as well as the experimentally relevant aspects describing the interaction between QDs and light.

5.1.1 Effective-Mass Theory

The commonly employed bandstructure method for QDs is the effective-mass theory. It assumes that the bands, which are exact solutions in the bulk semiconductor, are weakly perturbed by the nanostructure. Formally, a quantized eigenstate within an electronic band can be written as a product of a periodic Bloch function, $u(\mathbf{r})$, which captures the properties on the length scale of the crystal unit cell, and a slowly varying envelope, $\psi(\mathbf{r})$, that inherits the size and symmetry of the mesoscopic QD potential

$$\Psi_j(\mathbf{r}) = \psi_j(\mathbf{r})u_j(\mathbf{r}), \quad (5.1)$$

where $j = \{e, hh, lh\}$ labels either of the three relevant bands in zincblende semiconductors: electron, heavy hole, and light hole, respectively. It can be shown [40] that ψ_j is subject to a Schrödinger-type equation

$$E_j\psi_j(\mathbf{r}) = -\frac{\hbar^2}{2m_{\text{eff},j}}\Delta\psi_j(\mathbf{r}) + V_j(\mathbf{r})\psi_j(\mathbf{r}), \quad (5.2)$$

where we assume that the effective mass is isotropic. The complicated unit-cell potential is merged into the effective mass, m_{eff} , a parameter that can be inferred from experiments. The potential energy $V_j(\mathbf{r})$ contains the smooth mesoscopic potential of the QD as illustrated in Fig. 5.1. This particle-in-a-box problem can be solved either analytically or numerically using the standard techniques of quantum mechanics.

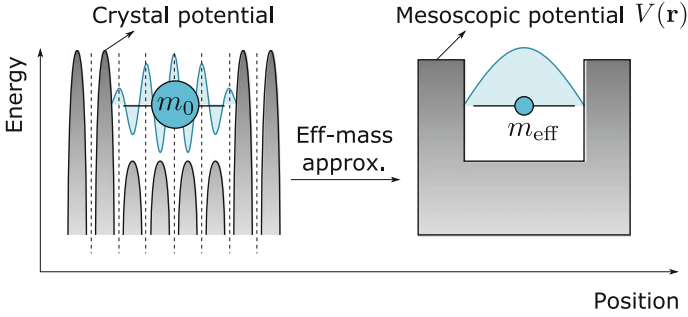


Fig. 5.1 Physical interpretation of the effective-mass approximation. The complicated crystal potential (*left*) is merged into an effective-mass parameter (*right*)

The effective-mass theory describes the properties of QDs remarkably well, since the first valence-band eigenstate is usually heavy-hole-like with a negligible light-hole component. This is related to the presence of compressive strain in In(Ga)As/GaAs QDs, which alters the symmetry of the unit cells and splits the degeneracy of the bands [41]. In strain-free QDs, the ground state is still mostly heavy-hole like due to the small aspect ratio of QDs [24, 36, 42–44].

5.1.2 Excitons

Electrons and holes possess charge and half-integer spin and therefore interact. The electron-hole bound state constitutes a fundamental quasi-particle, the exciton, which governs the optical properties of QDs. Being a two-body system, the exciton wavefunction Ψ_X can be expanded in the single-particle electron and hole wavefunctions [45]

$$\Psi_X(\mathbf{r}_e, \mathbf{r}_h) = \sum_{n,m} C_{n,m} \Psi_n^e(\mathbf{r}_e) \Psi_m^h(\mathbf{r}_h) = u_e(\mathbf{r}_e) u_h(\mathbf{r}_h) \psi_X(\mathbf{r}_e, \mathbf{r}_h), \quad (5.3)$$

where Ψ_n corresponds to the n -th eigenstate of the QD and $\psi_X(\mathbf{r}_e, \mathbf{r}_h)$ is the slowly varying envelope of the exciton subject to the two-body effective-mass Schrödinger equation

$$\left(\frac{\mathbf{p}_e^2}{2m_e} + \frac{\mathbf{p}_h^2}{2m_h} + V_e(\mathbf{r}_e) + V_h(\mathbf{r}_h) - \frac{e^2}{4\pi\epsilon_0\epsilon|\mathbf{r}_e - \mathbf{r}_h|} \right) \psi_X = E\psi_X. \quad (5.4)$$

Here, \mathbf{p} is the momentum operator, ϵ_r is the dielectric constant and E the energy of the exciton. In bulk, the electron and hole orbit each other within a distance known as the exciton Bohr radius a_0 . Since the Coulomb energy E_C scales inversely with the

QD size, $E_C \propto L^{-1}$, the Coulomb and exchange interactions in a QD are enhanced compared to bulk. On the other hand, the quantum-confinement energy scales as L^{-2} . As a consequence, the exciton motion can be found in two regimes:

(i) The *strong-confinement regime*, in which $L \ll a_0$ [46] and quantum confinement dominates Coulomb confinement. The latter can be neglected and the electron and hole therefore move independently as non-interacting particles $\psi_{\mathbf{x}}(\mathbf{r}_e, \mathbf{r}_h) = \psi_e(\mathbf{r}_e)\psi_h(\mathbf{r}_h)$. Most of the studied semiconductor QDs in the literature are in the strong-confinement regime. The dipole moment of an x -polarized exciton is

$$\boldsymbol{\mu} = \frac{e}{m_0} \langle \Psi_h | \hat{p}_x | \Psi_e \rangle \mathbf{e}_x \simeq \frac{e}{m_0} p_{cv} \langle \psi_h | \psi_e \rangle \mathbf{e}_x, \quad (5.5)$$

where \mathbf{e}_x is the Cartesian unit vector, $p_{cv} = V_{\text{UC}}^{-1} \int_{\text{UC}} d^3\mathbf{r} u_x^* \hat{p}_x u_e$ is the interband Bloch matrix element with V_{UC} being the unit-cell volume. In the above equation we have exploited the slow variation of the envelopes ψ over one unit cell. The dipole moment of small QDs has therefore an upper limit of $\mu_{\text{max}} = (e/m_0) p_{cv}$.

(ii) The *weak-confinement regime*, in which $L \gtrsim a_0$ and the electron-hole motion is correlated. Here, (5.4) has to be solved as a two-body problem. Achieving this regime has been a long-sought goal in quantum photonics because such QDs exhibit a giant dipole moment beyond μ_{max} , cf. Sect. 5.3.

Excitonic effects have a prominent role in determining the QD energy structure. Combining the electron contribution with a spin of $\pm 1/2$ with the heavy-hole projected angular momentum of $\pm 3/2$ yields four possible excitonic configurations: two optically bright with $j_z = \pm 1$ and two optically dark with $j_z = \pm 2$. Bright excitons are higher in energy than dark excitons by several hundred μeV [47]. The splitting between the two bright states is of the order of tens of μeV [47] and is mostly determined by the QD asymmetry [48]. The resulting dipole moments of the bright excitons $j_z = \pm 1$ are orthogonally polarized along the $x = [1, 1, 0]$ and $y = [1, -1, 0]$ crystallographic directions.

5.1.3 Spontaneous Emission

The light-matter interaction strength governs the temporal dynamics of the exciton-to-photon conversion. In the Wigner–Weisskopf approximation, the QD exciton decays exponentially with the rate Γ_{rad} determined by Fermi's Golden Rule

$$\Gamma_{\text{rad}} = \frac{2\pi}{\hbar^2} \sum_f |\langle f | \hat{H}_{\text{int}} | i \rangle|^2 \delta(\omega - \omega_{if}), \quad (5.6)$$

where \hat{H}_{int} is the light-matter interaction Hamiltonian triggering a transition from the initial $|i\rangle$ to the final $|f\rangle$ state. In this work we consider the minimal-coupling interaction Hamiltonian [49] between an electron with charge e and mass m_0 ,

and the field described by the vector potential $\hat{\mathbf{A}}$

$$\hat{H}_{\text{int}} = -\frac{e}{2m_0} \left(\hat{\mathbf{p}} \cdot \hat{\mathbf{A}} + \hat{\mathbf{A}} \cdot \hat{\mathbf{p}} - e\hat{\mathbf{A}} \cdot \hat{\mathbf{A}} \right). \quad (5.7)$$

Another commonly used Hamiltonian is the multipolar Hamiltonian, which is expressed in terms of electric and magnetic fields. It can be shown [49] that the two Hamiltonians give the same result for energy conserving processes such as spontaneous emission [50].

The nonlinear term $\hat{\mathbf{A}} \cdot \hat{\mathbf{A}}$ can be neglected for the weak fields studied here. We employ the generalized Coulomb gauge, $\nabla \cdot [\epsilon(\mathbf{r})\hat{\mathbf{A}}(\mathbf{r})] = 0$, yielding

$$\hat{H}_{\text{int}} \simeq -\frac{e}{m_0} \hat{\mathbf{A}}(\mathbf{r}) \cdot \hat{\mathbf{p}}, \quad (5.8)$$

where the dielectric constant $\epsilon(\mathbf{r})$ is assumed to vary over length scales larger than the QD size [51]. The vector potential can be written in terms of the normal field modes [52]

$$\hat{\mathbf{A}}(\mathbf{r}) = \sum_l \sqrt{\frac{\hbar}{2\epsilon_0\omega_l}} \left[\hat{a}_l \mathbf{f}_l(\mathbf{r}) + \hat{a}_l^\dagger \mathbf{f}_l^*(\mathbf{r}) \right], \quad (5.9)$$

where \hat{a}_l (\hat{a}_l^\dagger) is the annihilation (creation) operator for the l mode. The QD is approximated as a two-level system with the initial state $|i\rangle = |e\rangle \otimes |0\rangle$ with the exciton in the excited state $|e\rangle$ and the field in the ground state $|0\rangle$, and $|f\rangle = |g\rangle \otimes |1_f\rangle$ the final state with one excitation in the field mode f and the emitter in the ground state $|g\rangle$. Plugging this into (5.6) yields

$$\Gamma_{\text{rad}} = \frac{\pi e^2}{\epsilon_0 \hbar m_0^2} \sum_l \frac{1}{\omega_l} |\langle g | \mathbf{f}_l^*(\mathbf{r}) \cdot \hat{\mathbf{p}} | e \rangle|^2 \delta(\omega - \omega_l), \quad (5.10)$$

which is the starting point for the research presented here. The expression is beyond the dipole approximation because the variation of the field over the emitter is taken into account.

5.1.4 The Dipole Approximation: Oscillator Strength and Density of Optical States

The standard-textbook approach to evaluating (5.10) is to assume that the field does not vary over the QD, $\mathbf{f}_l(\mathbf{r}) \approx \mathbf{f}_l(\mathbf{r}_0)$, where \mathbf{r}_0 is the QD center. The resulting dipole approximation is excellent for quantum emitters that are much smaller than the wavelength of light. We thus obtain

$$\Gamma_{\text{rad}} = \frac{\pi |\boldsymbol{\mu}|^2}{\epsilon_0 \hbar} \mathbf{e}_p \cdot \left[\sum_l \frac{1}{\omega_l} \mathbf{f}_l^*(\mathbf{r}_0) \mathbf{f}_l(\mathbf{r}_0) \delta(\omega - \omega_l) \right] \cdot \mathbf{e}_p^*, \quad (5.11)$$

where \mathbf{e}_p is the unit vector pointing along the direction of the dipole moment. The term in square brackets is proportional to the imaginary part of the Green tensor [25, 52]

$$\text{Im} \underline{\underline{\mathbf{G}}}(\mathbf{r}, \mathbf{r}') = \frac{\pi c_0^2}{2} \sum_l \frac{1}{\omega_l} \mathbf{f}_l^*(\mathbf{r}) \mathbf{f}_l(\mathbf{r}') \delta(\omega - \omega_l), \quad (5.12)$$

In the dipole approximation, the light-matter interaction strength is thus governed by two quantities: the dipole moment $\boldsymbol{\mu}$, which is an intrinsic property of the emitter, and the imaginary part of the Green tensor, which is a property of the electromagnetic environment.

It is often useful to recast the emitter and field properties in terms of the oscillator strength f and the projected local density of optical states (LDOS) $\rho(\mathbf{r}_0, \omega, \mathbf{e}_p)$. The oscillator strength is a dimensionless quantity defined as the ratio between the radiative rate of the QD in a homogeneous environment and the emission rate of a classical harmonic oscillator, and is related to the dipole moment via

$$f = \frac{m_0}{e^2 \hbar \omega} |\boldsymbol{\mu}|^2. \quad (5.13)$$

The oscillator strength of atoms is of the order of 1 and about 10 for QDs [53] because QDs are larger and interact stronger with light. Conventional QDs are in the strong-confinement regime with a maximum oscillator strength of

$$f_{\text{max}} = \frac{E_g}{\hbar \omega}, \quad (5.14)$$

where E_g is the Kane energy, an experimentally accessible quantity. This upper limit for f can be understood from (5.5), where the overlap between the envelopes cannot exceed unity. The LDOS is defined as the number of electromagnetic modes per unit energy and volume that the emitter can decay into

$$\rho(\mathbf{r}_0, \omega, \mathbf{e}_p) = \frac{2\omega}{\pi c_0^2} \text{Im} \left[\mathbf{e}_p \cdot \underline{\underline{\mathbf{G}}}(\mathbf{r}_0, \mathbf{r}_0) \cdot \mathbf{e}_p^* \right]. \quad (5.15)$$

Modern fabrication techniques enable accurate tailoring of the LDOS surrounding the QDs in, e.g., photonic-crystal cavities [54] and waveguides [10], micropillar cavities [55], nanowires [7] and plasmonic nano-antennas [56].

In a homogeneous medium, the Green tensor can be evaluated analytically [52] yielding

$$\Gamma_{\text{rad}}^{\text{hom}} = \frac{\mu_0 \omega n}{3\pi \hbar c_0} |\boldsymbol{\mu}|^2. \quad (5.16)$$

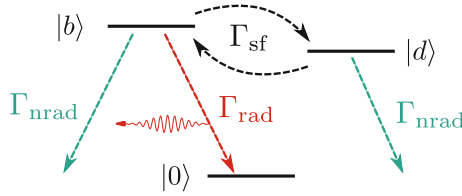


Fig. 5.2 Level scheme describing the population transfer of the exciton in a QD. The bright exciton $|b\rangle$ can decay either radiatively (Γ_{rad}) or nonradiatively (Γ_{nrad}) and can interact with its the dark exciton $|d\rangle$ via the spin-flip rate (Γ_{sf}). Figure reproduced from [42]

Finally we note that only the imaginary part of the Green tensor contributes to the decay rate because energy dissipation is described by the part of the response function, which is $\pi/2$ out of phase with the driving field, as is known for the harmonic oscillator. The real part is proportional to a self-energy term, the Lamb shift, which shifts the frequency of the QD exciton [57].

5.1.5 Decay Dynamics of Quantum Dots

The internal structure of QDs is more complicated than a two-level system: there are 4 excited states comprising 2 bright and 2 dark excitons, which are coupled by spin-flip processes. Furthermore, the omnipresent nonradiative processes, such as defect traps in the vicinity of the QD [58], provide alternative pathways for the recombination of the exciton. The experimentally measured decay rates of QDs therefore depend on radiative, nonradiative, and spin-flip processes. Analyzing the dynamics provides important information about the optical quality of QDs, namely the oscillator strength and the quantum efficiency η . The latter quantifies the probability that the QD exciton recombines radiatively

$$\eta = \frac{\Gamma_{rad}^{hom}}{\Gamma_{rad}^{hom} + \Gamma_{nrad}}, \quad (5.17)$$

where Γ_{nrad} is the nonradiative rate. In the following we present a method that can unambiguously extract these quantities from measurements [23, 42, 53].

Spin-flip processes are inhibited in QDs because it is difficult to simultaneously flip spin and fulfil energy conservation due to the discrete spectrum. The coupling between bright-bright and dark-dark excitons can generally be neglected because it is a second-order process. Only bright-dark excitons are coupled by Γ_{sf} and the level scheme is reduced to the one depicted in Fig. 5.2. Bright-dark and dark-bright spin-flip rates are assumed to be the same because the thermal energy at 4–10 K is larger than the bright-dark energy splitting. Also, the nonradiative rates of bright and dark excitons are the same due to their small energy splitting [59].

The decay dynamics of the bright exciton is governed by the rate equations of the coupled three-level system

$$\begin{bmatrix} \dot{\rho}_B \\ \dot{\rho}_D \end{bmatrix} = \begin{bmatrix} -\Gamma_{\text{rad}} - \Gamma_{\text{nrad}} - \Gamma_{\text{sf}} & \Gamma_{\text{sf}} \\ \Gamma_{\text{sf}} & -\Gamma_{\text{nrad}} - \Gamma_{\text{sf}} \end{bmatrix} \begin{bmatrix} \rho_B \\ \rho_D \end{bmatrix}, \quad (5.18)$$

where ρ denotes the occupation probability. Under the realistic assumption that spin flip-processes are much slower than the radiative rate, i.e., $\Gamma_{\text{sf}} \ll \Gamma_{\text{rad}}$, (5.18) yields for the decay of the bright state

$$\rho_B(t) = \rho_B(0)e^{-(\Gamma_{\text{rad}} + \Gamma_{\text{nrad}})t} + \frac{\Gamma_{\text{sf}}}{\Gamma_{\text{rad}}}\rho_D(0)e^{-(\Gamma_{\text{nrad}} + \Gamma_{\text{sf}})t}. \quad (5.19)$$

The bright exciton exhibits a biexponential decay with the fast rate $\Gamma_F = \Gamma_{\text{rad}} + \Gamma_{\text{nrad}}$ and the slow rate $\Gamma_S = \Gamma_{\text{nrad}} + \Gamma_{\text{sf}}$. Consequently, by fitting the measured decay curves with $f(\tau) = A_F e^{-\Gamma_F \tau} + A_S e^{-\Gamma_S \tau} + C$, where τ is the time delay with respect to the start of the excitation pulse and C is the background level, which is determined by the measured dark-count rate and after-pulsing probability of the detector, the radiative and nonradiative rates can be unambiguously extracted via

$$\Gamma_{\text{rad}} = \Gamma_F - \Gamma_S, \quad (5.20)$$

$$\Gamma_{\text{nrad}} = \Gamma_S - \frac{A_S}{A_F} \frac{\rho_B(0)}{\rho_D(0)} (\Gamma_F - \Gamma_S), \quad (5.21)$$

$$\Gamma_{\text{sf}} = \frac{A_S}{A_F} \frac{\rho_B(0)}{\rho_D(0)} (\Gamma_F - \Gamma_S). \quad (5.22)$$

For non-resonant excitation, QDs trap carriers with random spin, i.e.,

$$\frac{\rho_B(0)}{\rho_D(0)} \simeq 1. \quad (5.23)$$

Notably, the radiative rate Γ_{rad} does not coincide with the homogeneous-medium quantity $\Gamma_{\text{rad}}^{\text{hom}}$ because QDs are often located close to dielectric-dielectric or dielectric-air interfaces, which may modify the LDOS.

5.2 Light-Matter Interaction Beyond the Dipole Approximation with In(Ga)As Quantum Dots

The experimental observation of the dipole-theory breakdown was presented in [20], where QDs placed near a metal interface were probed by time-resolved photoluminescence measurements, cf. Fig. 5.3. In the experiment, the QD spontaneous-emission rate was found to be inhibited relative to the dipole theory for the geometry in

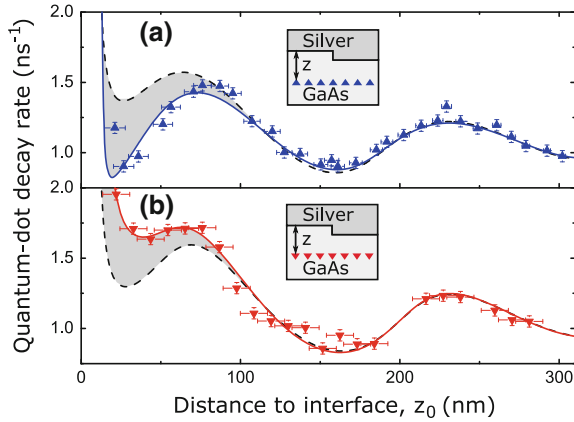


Fig. 5.3 Observation of deviations from the dipole theory for QDs near a metal interface [20]. The decay rate of QDs close to a metal interface was measured for **a** direct and **b** inverted QDs relative to the interface. The *black dashed line* denotes the dipole theory, the *triangles* the data points and the *colored solid lines* the fit. Figure reproduced from [20]

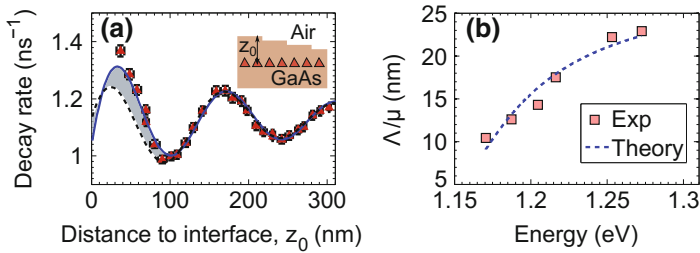


Fig. 5.4 Observation of deviations from the dipole theory for QDs near a dielectric interface. **a** Measured decay rates versus distance z_0 to the GaAs-air interface (data points) at an energy of 1.27 eV. The dipole (multipolar) theory is indicated by the *black dashed (blue solid) line*. A refractive index $n = 3.5$ of GaAs was used. **b** Extracted mesoscopic strength Λ/μ over the emission spectrum of QDs (*red squares*) along with the prediction of the theoretical model (*blue dashed line*). Figure reproduced from [22] (color figure online)

Fig. 5.3a. In contrast, the inverted structure in Fig. 5.3b showed an increase in the rate; the two structures would exhibit the same rates, if the QDs were dipoles. The observed difference is thus a direct demonstration of the breakdown of the dipole theory. The effects beyond the dipole approximation were merged into a phenomenological QD parameter, the mesoscopic moment $\Lambda = (e/m_0)\langle 0|x\hat{p}_z|\Psi_X\rangle$.

Deviations from the dipole theory have also been observed in the vicinity of an air interface [22, 53, 58], cf. Fig. 5.4, at distances below ~ 75 nm, which can again be explained by the mesoscopic moment Λ . The extracted mesoscopic strength Λ/μ increases with emission energy and varies from 10 to 23 nm over the inhomogeneously broadened emission spectrum, cf. Fig. 5.4b, and is successfully explained by our microscopic QD theory, which is presented later. The emission rate at the

air interface is enhanced while at the metal interface it is suppressed (for the direct structure) due to the phase shift gained upon reflection in the latter case, which flips the sign of the field gradient.

The QD wavefunctions obtained from the effective-mass theory cannot explain the large mesoscopic moment Λ observed experimentally. Sections 5.2.1–5.2.3 present such a theory that is applied to describe the spontaneous-emission process from QDs in Sect. 5.2.5. It is shown that the inhomogeneous quantum-current distribution makes QDs a probe of electric and magnetic fields.

5.2.1 Theory of Light-Matter Interaction Beyond the Dipole Approximation

The starting point for the theory is to account for the variation of the electromagnetic field over the size of the exciton wavefunction in (5.12). The decay rate of the emitter becomes

$$\Gamma(\omega) = \frac{2\mu_0}{\hbar} \int \int d^3\mathbf{r} d^3\mathbf{r}' \text{Im} \left[\mathbf{j}(\mathbf{r}) \cdot \underline{\underline{\mathbf{G}}}(\mathbf{r}, \mathbf{r}') \cdot \mathbf{j}^*(\mathbf{r}') \right]. \quad (5.24)$$

Here, we define the quantum-mechanical current density $\mathbf{j}(\mathbf{r})$ of the QD

$$\mathbf{j}(\mathbf{r}) = \frac{e}{m_0} \hat{\mathbf{p}} \Psi_X(\mathbf{r}, \mathbf{r}). \quad (5.25)$$

Unlike the dipole theory, where the effect of the environment on the emitter can be thought of as a self-interaction term at a single point \mathbf{r}_0 , here the self interaction occurs between all possible pairwise points $(\mathbf{r}, \mathbf{r}')$ within Ψ_X . We perform an expansion in the field modes, $f_l(\mathbf{r})$, because the integral formulation offers limited physical insight and is often computationally infeasible.

The transition moment from the ground to the excited state is defined as

$$T_{0X} = \frac{e}{m_0} \langle 0 | f_l^*(\mathbf{r}) \cdot \hat{\mathbf{p}} | \Psi_X \rangle. \quad (5.26)$$

Expanding the normal mode f_l around the QD center \mathbf{r}_0 yields

$$T_{0X} = T_{0X}^{(0)} + T_{0X}^{(1)} + T_{0X}^{(2)} + \dots \quad (5.27)$$

The electric-dipole term neglects the variation of the field over the emitter

$$T_{0X}^{(0)} = T_{0X}^{(\mu)} = f_l^*(\mathbf{r}_0) \langle 0 | \hat{\mu}_i | \Psi_X \rangle = f_l^*(\mathbf{r}_0) \mu_i, \quad (5.28)$$

where $\mu_i = \langle 0 | \hat{\mu}_i | \Psi_X \rangle$, $\hat{\mu}_i = (e/m_0) \hat{p}_i$ is the electric-dipole operator, and implicit summation over indices is used. The first-order contribution reads

$$T_{0X}^{(1)} = \partial_j f_i^*(\mathbf{r}_0) \Lambda_{ji}, \quad (5.29)$$

where $\Lambda_{ij} = (e/m_0) \langle 0 | x_i \hat{p}_j | \Psi_X \rangle$ is the first-order mesoscopic moment. $T_{0X}^{(1)}$ can be written as a sum of the electric-quadrupole, $T_{0X}^{(Q)}$, and magnetic-dipole, $T_{0X}^{(m)}$, contributions

$$T_{0X}^{(1)} = T_{0X}^{(Q)} + T_{0X}^{(m)} = \frac{1}{2} \partial_j f_i^*(\mathbf{r}_0) \langle 0 | \hat{Q}_{ij} | \Psi_X \rangle + [\nabla \times \mathbf{f}^*(\mathbf{r}_0)] \cdot \langle 0 | \hat{\mathbf{m}} | \Psi_X \rangle, \quad (5.30)$$

where $\hat{Q}_{ij} = (e/m_0) (x_i \hat{p}_j + \hat{p}_i x_j)$ is the electric-quadrupole and $\hat{\mathbf{m}} = e/(2m_0) \mathbf{r} \times \hat{\mathbf{p}}$ the magnetic-dipole operator.

The second order correction to the transition moment is

$$T_{0X}^{(2)} = \partial_j \partial_k f_i^*(\mathbf{r}_0) \Omega_{kji}, \quad (5.31)$$

where $\Omega_{ijk} = (e/2m_0) \langle 0 | x_i x_j \hat{p}_k | \Psi_X \rangle$ is the second-order mesoscopic moment. $T_{0X}^{(2)}$ can be rewritten in terms of electric-octupole, $T_{0X}^{(O)}$, and magnetic-quadrupole, $T_{0X}^{(M)}$, contributions

$$T_{0X}^{(2)} = T_{0X}^{(O)} + T_{0X}^{(M)} = \frac{1}{6} \partial_{jk}^2 f_i^*(\mathbf{r}_0) \langle 0 | \hat{O}_{ijk} | \Psi_X \rangle + \frac{1}{2} \partial_j [\nabla \times \mathbf{f}^*(\mathbf{r}_0)]_i \langle 0 | \hat{M}_{ij} | \Psi_X \rangle, \quad (5.32)$$

where $\hat{O}_{ijk} = (e/m_0) (x_k x_j \hat{p}_i + x_k \hat{p}_j x_i + \hat{p}_k x_j x_i)$ is the electric-octupole and $\hat{M}_{ij} = (e/3m_0) [x_j (\mathbf{r} \times \hat{\mathbf{p}})_i + (\mathbf{r} \times \hat{\mathbf{p}})_i x_j]$ the magnetic-quadrupole operator.

All in all, the multipole expansion to second order results in five contributions

$$T_{0X} = T_{0X}^{(0)} + T_{0X}^{(1)} + T_{0X}^{(2)} = T_{0X}^{(\mu)} + T_{0X}^{(Q)} + T_{0X}^{(m)} + T_{0X}^{(O)} + T_{0X}^{(M)} + \dots, \quad (5.33)$$

which are summarized in Table 5.1 and sketched in Fig. 5.5. The zeroth order has only electric-dipole contributions, while higher orders include terms of both electric and magnetic nature.

The multipolar expansion depends on the choice of the expansion point \mathbf{r}_0 [60, 61], which leads to an \mathbf{r}_0 -dependent decay rate. We find that by consistently collecting the expansion orders in the decay rate rather than in the multipolar moments, the rate

Table 5.1 Overview of the different contributions to the multipole expansion of T_{0X} up to second order

Order	Overall	Electric	Magnetic
0	$T_{0X}^{(0)} = \mu_i f_i^*$	$T_{0X}^{(\mu)} = \langle \hat{\mu}_i \rangle f_i^*$	—
1	$T_{0X}^{(1)} = \Lambda_{ji} \partial_j f_i^*$	$T_{0X}^{(Q)} = \frac{1}{2} \langle \hat{Q}_{ij} \rangle \partial_j f_i^*$	$T_{0X}^{(m)} = \langle \mathbf{m} \rangle \cdot [\nabla \times \mathbf{f}^*]$
2	$T_{0X}^{(2)} = \Omega_{kji} \partial_j \partial_k f_i^*$	$T_{0X}^{(O)} = \frac{1}{6} \langle \hat{O}_{ijk} \rangle \partial_j \partial_k f_i^*$	$T_{0X}^{(M)} = \frac{1}{2} \langle \hat{M}_{ij} \rangle \partial_j [\nabla \times \mathbf{f}^*]_i$

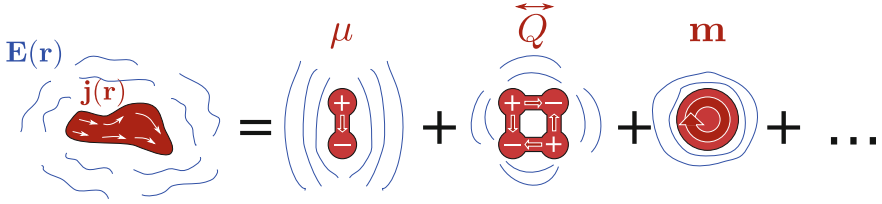


Fig. 5.5 Interpretation of the multipole expansion. The interaction between the current $\mathbf{j}(\mathbf{r})$ and field $\mathbf{E}(\mathbf{r})$ is decomposed into a linear superposition of multipoles

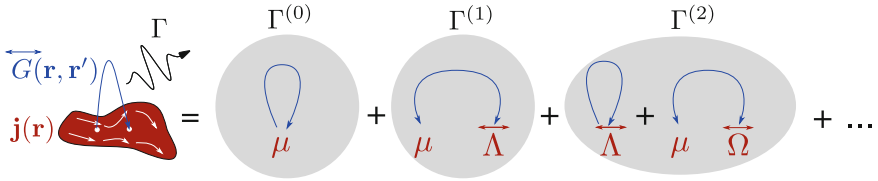


Fig. 5.6 Physical interpretation of the spontaneous-emission rate decomposed into the constituent multipoles. The nonlocal interaction between the points \mathbf{r} and \mathbf{r}' within the current density of the emitter is converted into an interaction between the different multipoles of the emitter

is remarkably robust against changes in \mathbf{r}_0 . For a detailed derivation the reader is referred to [50]. This aspect is of important for the justification of the multipolar expansion.

We expand Γ up to the second order because the first-order term vanishes in parity-symmetric environments

$$\Gamma \approx \Gamma^{(0)} + \Gamma^{(1)} + \Gamma^{(2)}. \tag{5.34}$$

The zeroth-order term stems from the dipole nature of the emitter (Fig. 5.6),

$$\begin{aligned} \Gamma^{(0)} &= \frac{\pi}{\epsilon_0 \hbar} \sum_l \frac{1}{\omega_l} |T_{0X}^{(0)}|_l^2 \delta(\omega - \omega_l) \\ &\stackrel{1,12}{=} \frac{2\mu_0}{\hbar} \text{Im} [\mu_i G_{ij}(\mathbf{r}_0, \mathbf{r}_0) \mu_j^*]. \end{aligned} \tag{5.35}$$

The first-order contribution reads

$$\begin{aligned} \Gamma^{(1)} &= \frac{\pi}{\epsilon_0 \hbar} \sum_l \frac{1}{\omega_l} 2\text{Re} T_{0X}^{(1)} T_{0X}^{(0)*} \delta(\omega - \omega_l) \\ &= \frac{2\mu_0}{\hbar} 2\text{Re} [\Lambda_{ki} \mu_j^*] \partial_k \text{Im} [G_{ij}(\mathbf{r}, \mathbf{r}_0)]|_{\mathbf{r}=\mathbf{r}_0}, \end{aligned} \tag{5.36}$$

and is proportional to the field gradient at the position of the emitter. $\Gamma^{(1)}$ can be interpreted as an interference between the dipole and mesoscopic quantities. Importantly, $\Gamma^{(1)} = 0$ if either the QD and/or environment are parity symmetric [21]. The dipole approximation is therefore protected by parity symmetry to first order.

The second-order contribution to the radiative rate is

$$\begin{aligned} \Gamma^{(2)} &= \frac{\pi}{\epsilon_0 \hbar} \sum_l \frac{1}{\omega_l} \left[2\text{Re} T_{0X}^{(2)} T_{0X}^{(0),*} + T_{0X}^{(1)} T_{0X}^{(1),*} \right]_l \delta(\omega - \omega_l) \\ &= \frac{2\mu_0}{\hbar} \text{Im} \left\{ \left[2\text{Re} \Omega_{lki} \mu_j^* \partial_k \partial_l + \Lambda_{ki} \Lambda_{lj}^* \partial_k \partial_l' \right] G_{ij}(\mathbf{r}, \mathbf{r}') \Big|_{\mathbf{r}=\mathbf{r}'=\mathbf{r}_0} \right\}, \quad (5.37) \end{aligned}$$

and couples to the second-order derivative of the field. Here the first term stems from the interference between $\underline{\mu}$ and $\underline{\Omega}$, which share contributions with the same parity. In contrast, the second term vanishes for parity-symmetric emitters on dipole-allowed transitions because $\underline{\mu}$ and $\underline{\Lambda}$ are orthogonal.

The first-order mesoscopic moment $\underline{\Lambda}$ contains 9 entries and the second-order moment $\underline{\Omega}$ 27 entries. However, many vanish for symmetry reasons, and only a few capture the essential physics. Motivated by the shape of In(Ga)As QDs [24] we assume the QDs to be lens shaped with in-plane cylindrical symmetry but with no parity symmetry in the growth direction. Notably, this analysis is not bound to this particular QD shape and is also valid for pyramidal or elliptical QDs. The exciton state is in the strong-confinement regime [53] and, using the effective-mass theory, the electron Ψ_e and hole Ψ_h wavefunctions are modeled as

$$\begin{aligned} \Psi_e(\mathbf{r}) &= u_e(\mathbf{r})\psi_e(\mathbf{r}), \\ \Psi_h(\mathbf{r}) &= u_h(\mathbf{r})\psi_h(\mathbf{r}), \end{aligned} \quad (5.38)$$

where u_e (u_h) is the conduction- (valence-) band Bloch function, and $\psi(\mathbf{r})$ is the slowly varying envelope. For concreteness we consider the x -polarized exciton but note that the properties of the y -polarized exciton are analogous.

In the following, we investigate the first-order mesoscopic moment

$$\Lambda_{ki} = \frac{e}{m_0} \langle 0 | (x_k - x_{0,k}) \hat{p}_i | \Psi_X \rangle = \frac{e}{m_0} \langle u_x \psi_h | (x_k - x_{0,k}) \hat{p}_i | u_e \psi_e \rangle. \quad (5.39)$$

The choice of x_0 and y_0 is provided naturally by the cylindrical symmetry of the QD. We define z_0 as the z -component of the exciton center-of-mass coordinate [50]. The valence-band Bloch function $u_h = u_x$ inherits the odd symmetry (“ -1 ”) of the p_x orbital in the x -direction and even parity (“ $+1$ ”) in y and z ; u_e inherits the spherical symmetry of the s -orbital. The slowly varying envelopes ψ inherit the symmetry of the QD, cf. Table 5.2. Thus, only Λ_{xz} and Λ_{zx} contain non-zero entries. $\Lambda_{zx} = (e/m_0) \langle \psi_h | z \hat{p}_x | \psi_e \rangle$ can be neglected because it couples to the QD height, which is much smaller than the in-plane size [24], yielding

Table 5.2 Symmetries of the electron and hole wavefunctions for a lens-shaped QD. ‘1’ denotes even parity, ‘-1’ odd parity and ‘0’ no parity

	u_x	ψ_h	Ψ_h	u_e	ψ_e	Ψ_e
x	-1	1	-1	1	1	1
y	1	1	1	1	1	1
z	1	0	0	1	0	0

$$\underline{\underline{\Lambda}} \simeq \begin{bmatrix} 0 & 0 & \Lambda \\ 0 & 0 & 0 \\ 0 & 0 & 0 \end{bmatrix}, \quad (5.40)$$

where $\Lambda \equiv \Lambda_{xz}$. Large values of $\Lambda/\mu \simeq 10\text{--}20\text{ nm}$ were measured for In(Ga)As QDs, cf. Fig. 5.4. With similar arguments it can be shown [50] that all the entries in $\underline{\underline{\Omega}}$ have negligible contributions such that

$$\Gamma = \frac{2\mu_0}{\hbar} \text{Im} \left\{ [\mu^*, \Lambda^*] \left[\begin{array}{cc} G_{xx}(\mathbf{r}_0, \mathbf{r}_0), & \partial_x G_{xz}(\mathbf{r}, \mathbf{r}_0) \\ \partial'_x G_{zx}(\mathbf{r}_0, \mathbf{r}'), & \partial_x \partial'_x G_{zz}(\mathbf{r}, \mathbf{r}') \end{array} \right] \Big|_{\mathbf{r}=\mathbf{r}'=\mathbf{r}_0} \begin{bmatrix} \mu \\ \Lambda \end{bmatrix} \right\}. \quad (5.41)$$

In conclusion, QDs have an additional optical degree of freedom, the mesoscopic moment Λ , which, combined with the dipole moment μ , describes light-matter interaction with QDs.

5.2.2 Microscopic Model for Mesoscopic Quantum Dots

The mesoscopic moment Λ has been used as a phenomenological quantity so far with no clear relation to the microscopic origin. The large Λ observed experimentally cannot be reproduced by the effective-mass theory because the size of Λ is governed by the gradient of the QD wavefunction, while, according to the effective-mass theory, gradients can only originate from the envelope functions, and are negligibly small. This can be shown by evaluating Λ with the rules employed for evaluating μ , which is to assume that ψ varies slowly over a unit cell so that $\mu = (e/m_0) \langle \psi_h u_x | \hat{p}_x | u_e \psi_e \rangle \approx (e/m_0) p_{cv} \langle \psi_h | \psi_e \rangle$, where $p_{cv} = V_{\text{UC}}^{-1} \int_{\text{UC}} d^3 \mathbf{r} u_x^* \hat{p}_x u_e$ is given by an integral over the unit cell with V_{UC} being the unit-cell volume. A similar calculation yields for Λ

$$\Lambda = \frac{e}{m_0} \left[\langle \psi_h | x | \psi_e \rangle \langle u_x | \hat{p}_z | u_e \rangle_{\text{UC}} + \langle \psi_h | \psi_e \rangle \langle u_x | x \hat{p}_z | u_e \rangle_{\text{UC}} \right. \\ \left. + \langle \psi_h | x \hat{p}_z | \psi_e \rangle \langle u_x | u_e \rangle_{\text{UC}} + \langle \psi_h | \hat{p}_z | \psi_e \rangle \langle u_x | x | u_e \rangle_{\text{UC}} \right], \quad (5.42)$$

where $\langle \rangle_{\text{UC}} \equiv V_{\text{UC}}^{-1} \int_{\text{UC}} d^3 \mathbf{r}$ denotes integration over a unit cell. The first three contributions vanish for symmetry reasons. The fourth contribution is vanishingly small

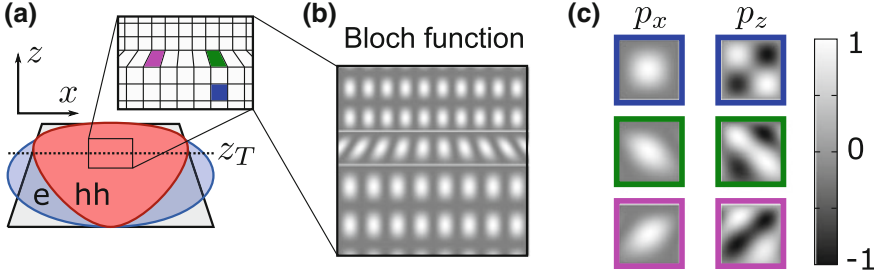


Fig. 5.7 Microscopic model for QDs. **a** The atomic lattice inside the QD is assumed to change periodicity at $z = z_T$. **b** Sketch of the spatial dependence of u_x^2 . **c** Illustration of the matrix elements $\langle p_x \rangle \equiv \langle u_x | \hat{p}_x | u_e \rangle$ and $\langle p_z \rangle \equiv \langle u_x | \hat{p}_z | u_e \rangle$ for the three colored unit cells in **a**. The symmetry of the integrand is broken in the transition region around $z = z_T$ giving rise to mesoscopic effects. Figure reproduced from [22]

and does not scale with the QD size: for Gaussian envelopes allowing for realistic mutual displacements of 1–2 nm between the electron and the hole in the growth direction (note that the integral vanishes in the absence of such a displacement) we estimate $\Lambda/\mu \sim 10^{-4}$ nm. In the following we develop a generalization of the effective-mass theory, and find that the mesoscopic moment originates from lattice inhomogeneities at the crystal-lattice level.

Using bulk-material Bloch functions works excellently for quantum wells and lattice-matched QDs, where the structures are strain free and structurally homogeneous. In(Ga)As QDs, on the other hand, are grown by strain relaxation, a violent process that unavoidably leads to the generation of structural gradients. In particular, large lattice-constant shifts are observed in the growth direction of QDs [24, 62]. Motivated by this we assume that the lattice periodicity changes at a certain position $z = z_T$ along the QD height by an amount $\Delta a_l = 110$ pm at a central value $a_l = 605$ pm as measured in [62], see Fig. 5.7a. The Bloch functions change periodicity as well, cf. Fig. 5.7b, and to describe this we expand them in a Fourier series with a position-dependent lattice wavevector $k_l(z)$

$$\begin{aligned} u_x(\mathbf{r}) &= \sum_m a_m(y, z) \sin[mk_l(z)x], \\ u_e(\mathbf{r}) &= \sum_n b_n(y, z) \cos[nk_l(z)x]. \end{aligned} \quad (5.43)$$

This Ansatz ensures opposite parity of the conduction- and valence-band Bloch functions along x . We assume the shape of the Bloch functions to be the same, and only their periodicity to vary. This yields for the interband matrix element $p_{cv} = \langle u_x | \hat{p}_x | u_e \rangle_{\text{UC}}$

$$p_{cv} = \frac{i\hbar}{V_{\text{UC}}} \sum_n \int_{\text{UC}} d^3r a_n^*(\mathbf{r}) b_n(\mathbf{r}) n k_l(z) \sin^2[nk_l(z)x]. \quad (5.44)$$

We now evaluate the mesoscopic moment by separating the slowly and rapidly varying contributions

$$\Lambda = \frac{e}{m_0} \sum_{q=1}^N \psi_g^*(\mathbf{R}_q) X_q \psi_e(\mathbf{R}_q) \int_{\text{UC}} d^3r u_x^*(\mathbf{r}) \hat{p}_z u_e(\mathbf{r}), \quad (5.45)$$

where \mathbf{R}_q denotes the position of the q -th unit cell and N is the number of unit cells. In a homogeneous region of the QD (the blue unit cell in Fig. 5.7a) the unit-cell integrand of (5.45) is odd in x - and z -directions, cf. Fig. 5.7c, which leads to a vanishing integral. However, in the transition region around $z = z_T$ strong gradients are present, which destroy the parity of the integrand (see the pink and green unit cells in Fig. 5.7a, c) and generate a contribution to Λ . The z -polarized Bloch matrix element $\langle u_x | \hat{p}_z | u_e \rangle$ is evaluated as

$$\langle u_x | \hat{p}_z | u_e \rangle \simeq i\hbar \sum_{m,n} \int_{\text{UC}} d^3r a_m^*(\mathbf{r}) b_n(\mathbf{r}) \frac{\partial k_l(z)}{\partial z} \sin[mk_l(z)x] n_x \sin[nk_l(z)x], \quad (5.46)$$

yielding

$$\Lambda = \sum_{q=1}^N \psi_h^*(\mathbf{R}_q) X_q \psi_e(\mathbf{R}_q) \sum_{m,n} \int_{\text{UC}} d^3r a_m^*(\mathbf{r}) b_n(\mathbf{r}) \frac{\partial k_l}{\partial z} \sin[mk_l x] n_x (x + X_q) \sin[nk_l x].$$

We assume that $\partial_z k_l$ is slowly varying over an unit cell and pull it in front of the unit-cell integral. The term containing x vanishes because the integral is odd and we are left with

$$\frac{\Lambda}{\mu} = \frac{1}{k_l} \frac{\langle \psi_h(\mathbf{r}) | x^2 [\partial_z k_l(z)] | \psi_e(\mathbf{r}) \rangle}{\langle \psi_h(\mathbf{r}) | \psi_e(\mathbf{r}) \rangle}. \quad (5.47)$$

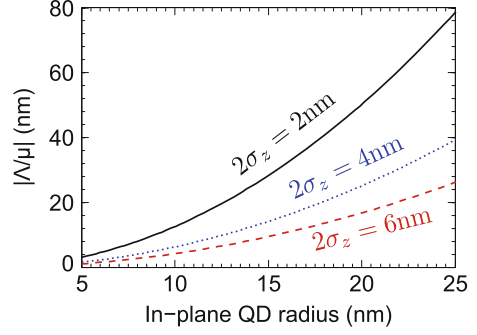
This expression shows that the mesoscopic strength scales quadratically with the in-plane size of the QD, $\Lambda/\mu \sim L_z^2$, because the term $\langle \psi_h | x^2 [\partial_z k_l(z)] | \psi_e \rangle$ contains the variance of the exciton wavefunction in the x -direction. Moreover, it increases with decreasing QD height, $\Lambda/\mu \sim L_z^{-1}$, since in shallow QDs the relative importance of the lattice-constant transition region is increased.

For in-plane rotationally symmetric Gaussian envelopes analytic expressions are obtained [22]

$$\frac{\Lambda}{\mu} = -\frac{\Delta a_l}{a_l} \sqrt{\frac{1 + \xi_z}{4\pi}} \frac{\sigma_r^2}{\sigma_z}, \quad (5.48)$$

where σ_z is the height (HWHM) of the electron envelope, σ_r the QD radius, $\Delta a_l/a_l$ the relative lattice-constant shift and $\xi_z \approx 5$ the ratio between the hole and electron effective masses. The largest mesoscopic strengths are achieved in shallow and wide (disk-shaped) QDs, cf. Fig. 5.8.

Fig. 5.8 The mesoscopic strength as a function of the in-plane size of the QD for three fixed QD heights. Figure reproduced from [22]



5.2.3 The Quantum Current Density of Quantum Dots

To illustrate the physics responsible for the mesoscopic moment we now calculate the quantum-mechanical current density resulting from the above model. The current density $\mathbf{j}_{\text{QD}}(\mathbf{r})$ flowing through the QD is defined in (5.25) and leads to

$$\mathbf{j}_{\text{QD}}(\mathbf{r}) = \frac{e}{m_0} [\Psi_h(\mathbf{r}) \hat{p}_x \Psi_e(\mathbf{r}) \mathbf{e}_x + \Psi_h(\mathbf{r}) \hat{p}_z \Psi_e(\mathbf{r}) \mathbf{e}_z]. \quad (5.49)$$

The current density $\mathbf{j}_{\text{QD}}(\mathbf{r}) = \mathbf{J}_{\text{QD}}(\mathbf{r}) p(\mathbf{r})$ is modulated by the Bloch element $p(\mathbf{r}) = u_x(\mathbf{r}) \hat{p}_x u_e(\mathbf{r})$. In the following we discuss the slowly varying component $\mathbf{J}_{\text{QD}}(\mathbf{r})$, which can be written as

$$\mathbf{J}_{\text{QD}}(\mathbf{r}) = \frac{e}{m_0} \psi_h(\mathbf{r}) \psi_e(\mathbf{r}) \left(\mathbf{e}_x + x \frac{1}{k_l} \frac{\partial k_l}{\partial z} \mathbf{e}_z \right). \quad (5.50)$$

We assume that most of the transition happens over two lattice constants as shown in [24]. In QDs with a homogeneous crystal lattice $\partial k_l / \partial z = 0$ and thus $\Lambda = 0$, the current density flows only along the direction of the dipole moment (see Fig. 5.9a). The presence of lattice inhomogeneities changes the flow due to transverse gradients. The current density flows along a curved path as illustrated in Fig. 5.9b–d. The wider the QD is, the sharper the transverse oscillations of the current are, and the larger Λ / μ is.

We now have the ingredients to provide an intuitive understanding of the experimental data in Fig. 5.3. In the direct (inverted) structure, Fig. 5.3a (Fig. 5.3b), the QD current and the plasmonic field flow along opposite (parallel) curvatures, which leads to enhanced (suppressed) light-matter interaction. We exemplify this for a silver nanowire with a radius of 20 nm and refractive index $n_{\text{Ag}} = 0.2 + 7i$, see Fig. 5.10. The coupling efficiency to plasmons, β_{pl} , is defined as the coupling rate to plasmons over the coupling rate to all excitations, which include photons, plasmons and ohmic losses. The configuration in Fig. 5.10a exhibits a larger coupling to surface plasmons relative to a dipole (from 75% to 90%), cf. Fig. 5.10c. In contrast, the interaction is diminished if the QD orientation is flipped, cf. Fig. 5.10b, because the QD current

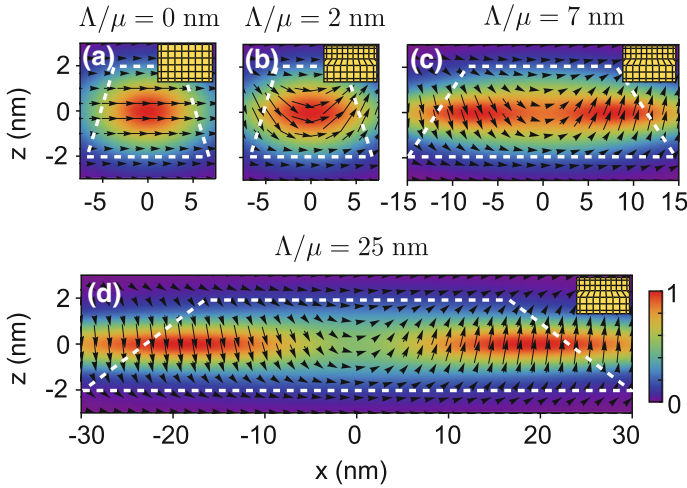


Fig. 5.9 Spatial distribution of the current density $J_{\text{QD}}(\mathbf{r})$ in QDs. **a** Homogeneous crystal lattice where the flow is uniform and points along the dipole moment. **b** Inhomogeneous lattice for a QD radius of 5 nm giving rise to a non-uniform flow along a curved path. The QD height is $2\sigma_z = 4$ nm. **c, d** Same as **b** but for QD radii of 10 and 20 nm, respectively. Both the length of the *arrows* and the color scale indicate the magnitude of the flow and the direction of the *arrows* indicates the pointwise direction of the flow. Figure reproduced from [22]

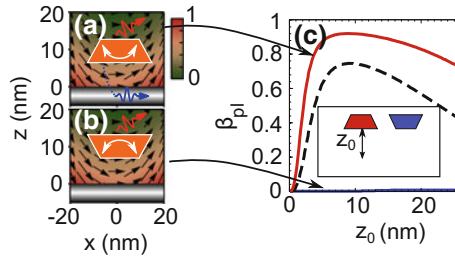


Fig. 5.10 QDs coupled to surface plasmons of a silver nanowire. **a** The field matches the curvature of the QD current and the coupling efficiency to surface plasmons, β_{pl} , is enhanced, *red curve* in **c**, relative to a dipole, *dashed curve* in **c**. **b** If the QD orientation is flipped, the interaction is diminished as shown in **c** by the *blue line*

and of the field oscillate in opposite directions. In other words, μ and Λ interfere constructively in (a) and destructively in (b).

5.2.4 Lattice-Distortion Effects Beyond the Multipolar Theory

Knowing the full current distribution according to the microscopic model allows to calculate the decay rate without relying on the multipolar expansion. Inserting (5.50)

into (5.24) leads to

$$\Gamma = \frac{2\mu_0 |p_{cv}|^2}{\hbar} \text{Im} \iint d^3r d^3r' [J_x(\mathbf{r}) \ J_z(\mathbf{r})] \begin{bmatrix} G_{xx}(\mathbf{r}, \mathbf{r}') & G_{xz}(\mathbf{r}, \mathbf{r}') \\ G_{zx}(\mathbf{r}, \mathbf{r}') & G_{zz}(\mathbf{r}, \mathbf{r}') \end{bmatrix} \begin{bmatrix} J_x^*(\mathbf{r}') \\ J_z^*(\mathbf{r}') \end{bmatrix}, \quad (5.51)$$

where $J_x(\mathbf{r}) = (e/m_0)\psi_h(\mathbf{r})\psi_e(\mathbf{r})$ and $J_z(\mathbf{r}) = xk_l^{-1}(\partial k_l/\partial z)J_x$. The zeroth order expansion of G_{xx} contains the electric-dipole contribution $\Gamma^{(0)}$. The other terms are generated by the transverse oscillations of the current density and contain the first $\Gamma^{(1)}$ and second $\Gamma^{(2)}$ order contributions. Equation (5.51) should be preferred over the multipolar theory when the figure of merit $k \times \Lambda/\mu > 1$, i.e., when the multipolar expansion diverges.

5.2.5 Quantum Dots as Probes for the Magnetic Field of Light

Electric and magnetic fields play an equally important role in the formation of the light field but interact fundamentally different with matter. The magnetic force acting on a charged particle with velocity v is v/c times smaller than the electric force. Magnetic light-matter interaction is therefore weak. Nevertheless, magnetic-dipole transitions are well known in atomic physics and can be accessed with light despite being weak [63–65], since they have different selection rules than electric-dipole transitions because atoms have parity symmetry [26, 27, 66]. The lack of parity symmetry implies that QDs may be exploited as a probe of electric and magnetic fields on a single electronic transition. We exemplify this by considering again the spontaneous emission of a QD in front of a metal interface [21]. The QD decays into propagating photons with the rate Γ_{RAD} , propagating surface plasmons (Γ_{PL}), or ohmic-lossy modes in the metal (Γ_{LS}) [67]. Γ_{RAD} is negligibly affected by the mesoscopic moment since the radiative modes oscillate weakly, i.e., $\Gamma_{\text{RAD}} \approx \Gamma_{\text{RAD}}^{(0)}$. In contrast, the plasmon field varies strongly in space and Λ plays a major role in the excitation rate of plasmons. The coupling to ohmic losses [68, 69] is normally negligible at distances larger than ~ 20 nm from the metal and are not discussed further. The three light-matter interaction channels are

$$\begin{aligned} \Gamma^{(0)} &= \frac{2\mu_0}{\hbar} \mu^2 \text{Im} G_{xx}(0, 0) = \Gamma_{\text{RAD}} + \Gamma_{\text{PL}}^{(0)}, \\ \Gamma^{(1)} &= \frac{2\mu_0}{\hbar} 2\Lambda\mu \partial_x \text{Im} G_{zx}(\mathbf{r}, 0)|_{r=0} \approx \Gamma_{\text{PL}}^{(1)}, \\ \Gamma^{(2)} &= \frac{2\mu_0}{\hbar} \Lambda^2 \partial_x \partial'_x \text{Im} G_{zz}(\mathbf{r}, \mathbf{r}')|_{r=r'=0} \approx \Gamma_{\text{PL}}^{(2)}, \end{aligned} \quad (5.52)$$

where we assume the QD wavefunctions to be real. Each order has a clear physical meaning as explained in Sect. 5.2.1 and can be visualized in Fig. 5.11.

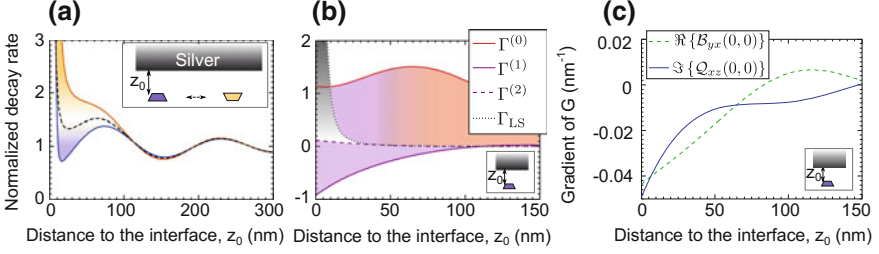


Fig. 5.11 Decay dynamics of QDs near a silver interface. All the rates are normalized to the decay rate in homogeneous GaAs. **a** Decay rate for the direct (inverted) QD orientation marked by blue (orange) lines. The black dashed line denotes the dipole theory. **b** Decomposition of the decay rates according to the expansion order. The ohmic losses are indicated by the dotted black line. **c** The ED-MD and ED-EQ Green tensor probed by mesoscopic QDs and normalized to $\text{Im}G_{xx}(0, 0)$ in homogeneous GaAs. Figure reproduced from [21]

In the following we show that $\Gamma^{(1)}$ probes the magnetic field of light. The mesoscopic moment Λ can be decomposed into multipolar contributions

$$\Lambda_{xz}\partial_x e_{l,z}(0) = i\omega m_y b_{l,y}(0) + Q_{xz} [\partial_x e_{l,z}(0) + \partial_z e_{l,x}(0)], \quad (5.53)$$

where $m_y = \Lambda/2$ is the magnetic dipole, $Q_{xz} = \Lambda$ the electric quadrupole of the QD, and \mathbf{e} and \mathbf{b} are the electric- and magnetic-field modes, respectively. Consequently, $\Gamma^{(1)}$ intertwines the electric dipole, magnetic dipole and electric quadrupole of the QD. The multipolar contribution to $\Gamma^{(1)}$ is

$$\Gamma^{(1)} = \frac{2\hbar}{\mu_0} [\omega m_y \mu \text{Re} \mathcal{B}_{yx}(\mathbf{r}_0, \mathbf{r}_0) + A Q_{xz} \mu \text{Im} \mathcal{Q}_{xz}(\mathbf{r}_0, \mathbf{r}_0)], \quad (5.54)$$

where $\mathcal{B}_{yx}(\mathbf{r}_0, \mathbf{r}_0) = -i\omega^{-1} [\partial_x G_{zx}(\mathbf{r}, \mathbf{r}_0) - \partial_z G_{xx}(\mathbf{r}, \mathbf{r}_0)]_{\mathbf{r}=\mathbf{r}_0}$ is the magneto-electric Green tensor, and $\mathcal{Q}_{xz}(\mathbf{r}_0, \mathbf{r}_0) = [\partial_x G_{zx}(\mathbf{r}, \mathbf{r}_0) + \partial_z G_{xx}(\mathbf{r}, \mathbf{r}_0)]_{\mathbf{r}=\mathbf{r}_0}$ the electric dipole-quadrupole Green tensor. The probed fields are plotted in Fig. 5.11c for an emitter close to a silver interface, where the two components of the Green tensor vary over length scales of tens of nanometers, which is comparable to the QD size.

The mesoscopic moment can also be used to probe the parity symmetry of nanophotonic environments [21]. If placed in an unknown nanophotonic structure, the spontaneous-emission rate of the QD is generally given by $\Gamma_{\blacktriangle} \approx \Gamma_{\blacktriangle}^{(0)} + \Gamma_{\blacktriangle}^{(1)}$. By flipping the QD orientation, the dipole contribution is unchanged but the first-order term has opposite symmetry and changes sign, i.e., $\Gamma_{\blacktriangledown} \approx \Gamma_{\blacktriangledown}^{(0)} + \Gamma_{\blacktriangledown}^{(1)} = \Gamma_{\blacktriangle}^{(0)} - \Gamma_{\blacktriangle}^{(1)}$. As a consequence, both the projected Green tensor $\text{Im}\{G_{xx}(0, 0)\}$ and the spatial gradient $\partial_x \text{Im}\{G_{zx}(0, 0)\}$ can be extracted using (5.52).

5.3 Single-Photon Superradiance from a Monolayer-Fluctuation Quantum Dot

We address another mesoscopic property of QDs, the collective coupling to light in terms of superradiance. We show that the fundamental optical excitation of a weakly confining QD is a generalization of single-photon superradiance (SPS) [23]. The superradiant state is prepared deterministically with a laser pulse and reaches a five-fold collective light-matter enhancement.

5.3.1 Extending the Concept of Superradiance from Atomic Physics to Solid-State Emitters

In the following we make a formal connection between the proposal of Dicke regarding SPS in an ensemble of atoms [39] and collective light-matter enhancement in a semiconductor QD. We show that the giant oscillator strength of QDs and SPS are two equivalent phenomena.

If N emitters are placed closer than one wavelength apart, the emission dynamics of a shared electronic excitation is strongly enhanced in the symmetric SPS state [39]

$$|\Psi_s\rangle = \frac{1}{\sqrt{N}} \sum_j |g\rangle_1 |g\rangle_2 \dots |e\rangle_j \dots |g\rangle_N, \quad (5.55)$$

where the j -th emitter is in the excited state $|e\rangle$ and all others in the ground state $|g\rangle$. Remarkably, the state $|\Psi_s\rangle$ decays N times faster to the ground state than a single emitter. This state describes a non-interacting ensemble, where the excitation is bound to either of the emitters, cf. Fig. 5.12a. Harvesting such effects in practice is challenging due to the large size and harmonic spectrum of many ensembles, which decreases the collective enhancement and prohibits deterministic preparation, respectively. These limitations do not apply to QDs, which are small and anharmonic. However, another challenge emerges: in a system of interacting particles the wavefunctions of the underlying atoms overlap leading to delocalized excitations. This causes conventional QDs to be in the strong-confinement regime and thus to have relatively small oscillator strengths of about 10, despite that they consist of tens of thousands of atoms, cf. Fig. 5.12b.

The size of delocalized excitations is a fundamental property of semiconductors and is given by the size of an exciton. Enhancement of light-matter interaction can therefore be achieved only in QDs that confine excitons weakly [70], i.e., that are larger than the exciton radius. We study single GaAs monolayer-fluctuations QDs as sketched in Fig. 5.12c. Bound excitonic states are created by intentionally engineered monolayer fluctuations in a quantum well [38]. Exciton enhancement is achieved only in the plane, where the QD wavefunction is extended beyond the exciton radius.

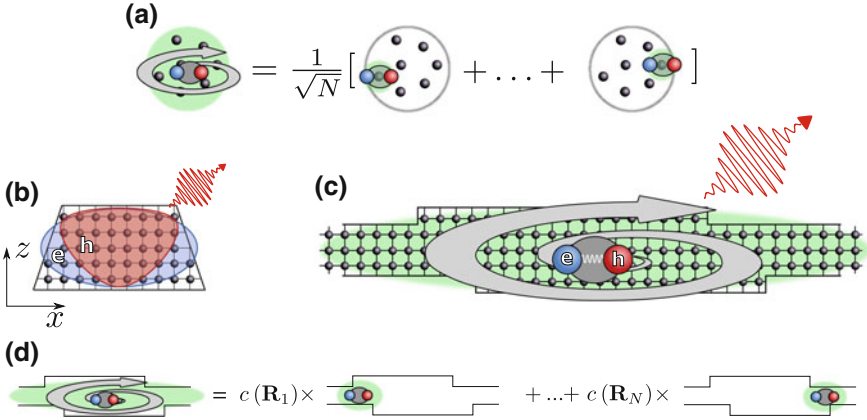


Fig. 5.12 Superradiance with single QDs. **a** SPS is defined in an ensemble of non-interacting emitters as a symmetric superposition of different excitations. **b** In small QDs, such as In(Ga)As QDs, the electrons and holes are strongly confined and uncorrelated, which destroys collective effects. **c** A QD defined by intentional monolayer fluctuations weakly confine electrons (e) and holes (h), which are mutually bound by electrostatic attraction. **d** The excitonic enhancement of light-matter interaction may be regarded as a generalization of SPS: the exciton is in a symmetric superposition of excitations. Figure reproduced from [23]

We assume the QD wavefunctions to be separable into in-plane ψ_X and out-of-plane ϕ components. Due to strong confinement in the z -direction, ϕ is separable as $\phi(z) = \phi_e(z)\phi_h(z)$. We therefore obtain the exciton wavefunction in the effective-mass approximation

$$\Psi_X(\mathbf{R}, \mathbf{r}, \mathbf{r}_e, \mathbf{r}_h) = \psi_X(\mathbf{R}, \mathbf{r})\phi_h(z_h)\phi_e(z_e)u_x(\mathbf{r}_h)u_e(\mathbf{r}_e), \quad (5.56)$$

where $\mathbf{R} = (m_e\mathbf{r}_e + m_h\mathbf{r}_h)/(m_e + m_h)$ and $\mathbf{r} = \mathbf{r}_e - \mathbf{r}_h$ are the center-of-mass and relative in-plane excitonic coordinates. The superradiant enhancement is therefore governed by the in-plane envelope $\psi_X(\mathbf{R}, \mathbf{r})$. We consider a symmetric parabolic in-plane confining potential, in which case the excitonic envelope separates into center-of-mass and relative dynamics $\psi_X(\mathbf{R}, \mathbf{r}) = \chi_{CM}(\mathbf{R})\chi_r(\mathbf{r})$ with [25]

$$\chi_{CM}(\mathbf{R}) = \sqrt{\frac{2}{\pi}} \frac{1}{\beta} e^{-|\mathbf{R}|^2/\beta^2}, \quad (5.57)$$

$$\chi_r(\mathbf{r}) = \sqrt{\frac{2}{\pi}} \frac{1}{a_{QW}} e^{-|r|/a_{QW}}, \quad (5.58)$$

where a_{QW} is the quantum-well exciton radius with $a_{QW} \simeq a_0/\sqrt{2} \approx 8$ nm, and β is the in-plane radius of the exciton wavefunction. The center-of-mass motion can be written as a convolution between a function $c_d(\mathbf{R})$ capturing the dynamics on the (uncorrelated) scale a_{QW} and a function $c_s(\mathbf{R})$ responsible for the superradiant

enhancement

$$\chi_{\text{CM}}(\mathbf{R}) = c_a(\mathbf{R}) * c_s(\mathbf{R}) \approx \sum_n c(\mathbf{R}_n) c_a(\mathbf{R} - \mathbf{R}_n). \quad (5.59)$$

Consequently, the slowly varying envelope reads

$$\psi_X(\mathbf{R}, \mathbf{r}) = \sum_n c(\mathbf{R}_n) \phi_X(\mathbf{R} - \mathbf{R}_n, \mathbf{r}), \quad (5.60)$$

where n runs over the unit cells of the QD. The internal exciton dynamics is governed by ϕ_X , which has a spatial extent of the order of the Bohr radius (~ 8 nm) and is smaller than the QD. The exciton in (5.60) is therefore in a spatial superposition of excitations corresponding to different positions of ϕ_X as illustrated in Fig. 5.12d.

The following expression for the oscillator strength is obtained (compare with (5.14))

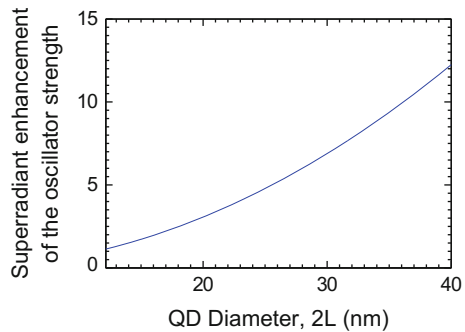
$$f = \frac{E_g}{\hbar\omega} \chi_r(0) |\langle 0 | \chi_{\text{CM}}(\mathbf{R}) \rangle|^2 |\langle \psi_h(z) | \psi_e(z) \rangle|^2, \quad (5.61)$$

where the first (second) inner product on the right-hand side of the equation denotes a two-dimensional (one-dimensional) integration over \mathbf{R} (z). We define the radius of the QD $L = \sqrt{2}\beta$ and, with the help of (5.57) and (5.58), arrive at the superradiant enhancement of the oscillator strength

$$S = \frac{f}{f_{\text{max}}} = \left(\frac{\sqrt{2}L}{a_{\text{QW}}} \right)^2 |\langle \psi_h | \psi_e \rangle|^2. \quad (5.62)$$

We calculate $|\langle \psi_h | \psi_e \rangle|^2 \approx 0.96$ and plot the resulting superradiant enhancement in Fig. 5.13. It scales with the QD area and is a dramatic effect; for realistic QD diameters of 35 nm, the light-matter interaction strength exceeds the upper limit of strongly confined excitons by an order of magnitude.

Fig. 5.13 Superradiant enhancement of the oscillator strength, S , for a monolayer-fluctuation QD relative to the strong-confinement limit $f_{\text{max}} = 17.4$. Figure reproduced from [23]



5.3.2 Deterministic Preparation and Impact of Nonradiative Processes

In the experimental demonstration of SPS, the energy-level structure of the QDs is first probed by photoluminescence-excitation spectroscopy as displayed in Fig. 5.14a, which shows a quasi-continuum band of QD states hybridized with quantum-well resonances followed by the exciton manifold. We identify the 1s, 2s and 3s excitonic states that are denoted according to the two-dimensional hydrogen atom. Note, the recombination of excitons with different symmetry is forbidden. Key features of the spectrum are summarized in Fig. 5.14b. The measurement was carried out using continuous-wave excitation below the saturation power of the 1s exciton.

Deterministic preparation is achieved by exciting the 2s state with a laser pulse having sufficient optical power to saturate the 1s transition. The preparation is deterministic because the decay cascade from 2s to 1s is spin-conserving [71] and spin-dark states are therefore not populated. However, the latter prohibits measurements of the oscillator strength due to the single-exponential character of the exciton decay. We therefore use another excitation scheme (the wavelength labeled “C” in Fig. 5.14) to prepare bright and dark states with equal probability and extract the impact of non-radiative processes using the biexponential model presented in Sect. 5.1.5.

Significantly below the exciton saturation, $P \approx 0.1P_{\text{sat}}$, only the exciton is prepared, cf. Fig. 5.15a. At saturation, the biexciton line becomes discernible. Above saturation, both the exciton and the biexciton lines are saturated and the spectrum features spectrally continuous multibody emissions. The nature of the exciton and biexciton lines is confirmed by power series measurements as shown in Fig. 5.15c.

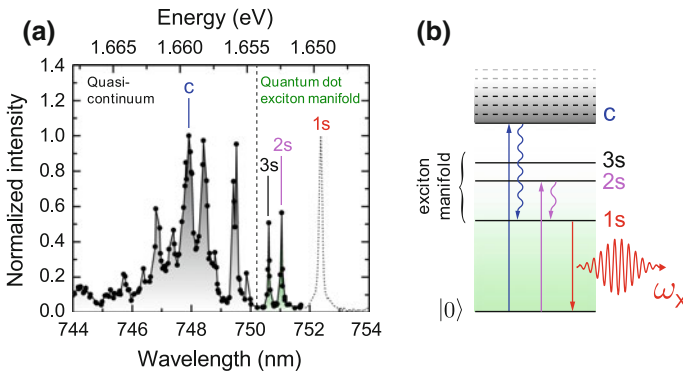


Fig. 5.14 Deterministic preparation of superradiant excitons. **a** Photoluminescence-excitation spectrum obtained by integrating the emission of the 1s transition while scanning the excitation wavelength. It features a quasi-continuum band of states followed by a sequence of QD states. **b** Two excitation schemes are employed. Pumping in the quasi-continuum band at the wavelength “C” results in preparation of carriers with random spin, which is important for extracting the nonradiative processes. For 2s-excitation, the spin is preserved and the bright exciton is prepared deterministically. Figure reproduced from [23]

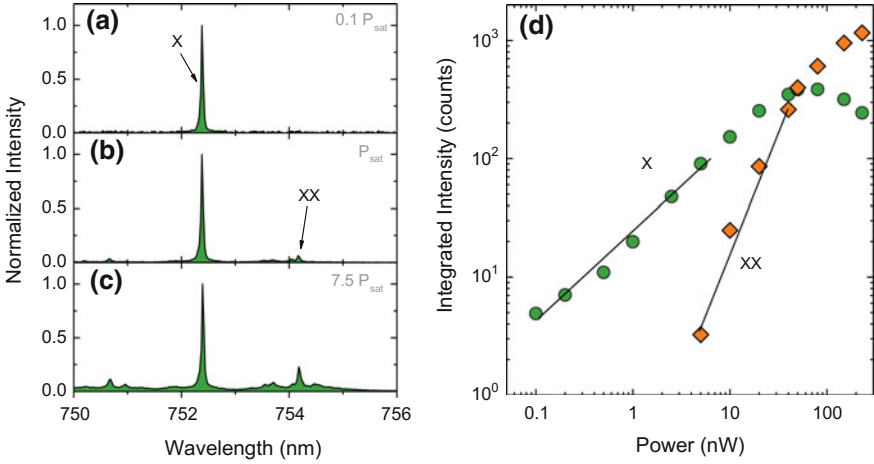


Fig. 5.15 Spectral measurements for “C”-excitation. **a** Measured spectrum at 10% of the exciton saturation power $P_{\text{sat}} = 20$ nW. Only the exciton is observed. **b** At saturation of the exciton, the biexciton is visible as a small peak. **c** Significantly above the exciton saturation ($7.5P_{\text{sat}}$), the spectrum acquires further narrow peaks on top of a continuous background. **d** The exciton is distinguished from biexcitons by their power-law dependence on excitation power P : the fits yield $P^{0.86}$ and $P^{2.01}$ for the exciton and biexciton, respectively

The spectral broadening of the biexciton line is related to multibody effects between the exciton and the free carriers populating the quantum well [35, 42].

The decay dynamics is recorded by sending the exciton line from Fig. 5.15a to an avalanche photo-diode. The acquired data are fitted by the biexponential model yielding the fast rate $\Gamma_F^C = \Gamma_{\text{rad}}^C + \Gamma_{\text{nr}}^C + \Gamma_{\text{sf}}$ and the extracted parameters are outlined in Fig. 5.16. We obtain a nonradiative rate $\Gamma_{\text{nr}}^C = 0.19 \text{ ns}^{-1}$, and a spin-flip rate $\Gamma_{\text{sf}} = 0.31 \text{ ns}^{-1}$, which are used to extract the oscillator strength in the following.

5.3.3 Demonstration of Single-Photon Superradiance

The experimental signature of SPS is spontaneous emission of single photons with a radiative rate beyond the upper limit for uncorrelated excitons. The 1s bright state is excited deterministically through the 2s shell and a clean emission spectrum below and at saturation is found. The time-resolved measurement is performed at $P = 0.1P_{\text{sat}}$ to ensure that no multi-exciton states are prepared, and the decay is found to be close to single exponential. The radiative rate of the exciton is $\Gamma_{\text{rad}} = \Gamma_F - \Gamma_{\text{nr}} - \Gamma_{\text{sf}} = 8.4 \text{ ns}^{-1}$, where Γ_F is the fast rate extracted from Fig. 5.17a. The QDs are positioned near an air interface [23] and we calculate an LDOS contribution of 0.95, which is normalized to the LDOS in homogeneous $\text{Al}_{0.8}\text{Ga}_{0.2}\text{As}$, resulting in an oscillator strength of $f = 72.7 \pm 0.8$. The latter is enhanced far beyond the upper

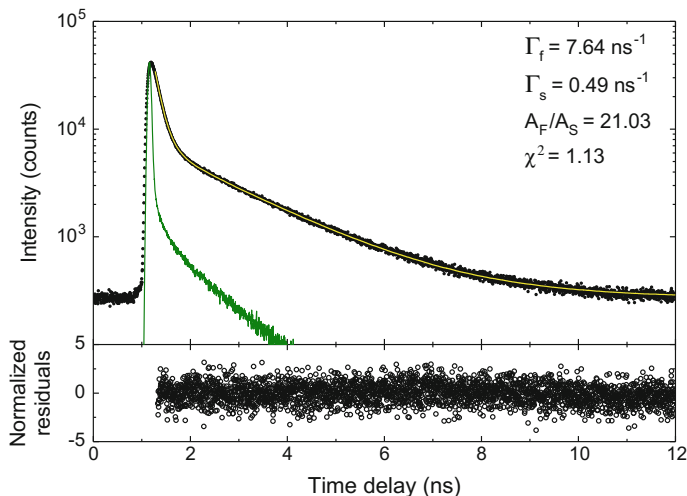


Fig. 5.16 Time-resolved decay of the exciton (*black dots*) under “C”-excitation. The fine-structure model yields an excellent biexponential fit (*yellow line*) with the extracted parameters indicated accordingly. The instrument response of the detector is indicated by the *green line*. Figure reproduced from [23] (color figure online)

limit of $f = 17.4$ for an uncorrelated exciton, cf. Fig. 5.17a. This is a direct signature of exciton superradiance.

To confirm the single-photon nature of the emission, we measure the second-order correlation function $g^{(2)}(\tau) \propto \langle \hat{a}^\dagger(t)\hat{a}^\dagger(t+\tau)\hat{a}(t+\tau)\hat{a}(t) \rangle$ [72], which determines the probability of detecting a photon at time $t = \tau$ given that a photon was detected at $t = 0$. An ideal single-photon source exhibits $g^{(2)}(0) = 0$ but any value below 0.5 is direct evidence of single photons. Figure 5.17b shows the correlation function obtained in an HBT experiment. The data are fitted by a sum of exponentially decaying functions, and $g^{(2)}(0)$ is defined by the ratio between the energy contained in the central peak around $\tau = 0$ and in the adjacent peaks. We find a zero-time correlation of $g^{(2)}(0) = 0.13$, demonstrating the single-photon nature of the emitted light. In conjunction with the measured enhanced oscillator strength for a spatially confined exciton, this is the unequivocal demonstration of SPS in a QD.

Solid-state quantum light sources often suffer from blinking of the emission, in which the QD randomly switches to a dark state and does not emit light [73]. This may happen, if a charge defect in the vicinity of the QD traps the electron or hole composing the exciton, thereby preventing the radiative recombination. This decreases the radiative efficiency of the single-photon source. Blinking normally occurs within nanosecond-to-microsecond time scales with a corresponding bunching in the QD second-order correlation function $g^{(2)}(\tau)$ over such time scales. By numerically integrating each peak in the HBT correlation data we obtain the long-time-scale plot shown in Fig. 5.17c. No bunching effects are observed, which shows that this single-photon source is free from blinking on a time scale of at least 10 μ s.

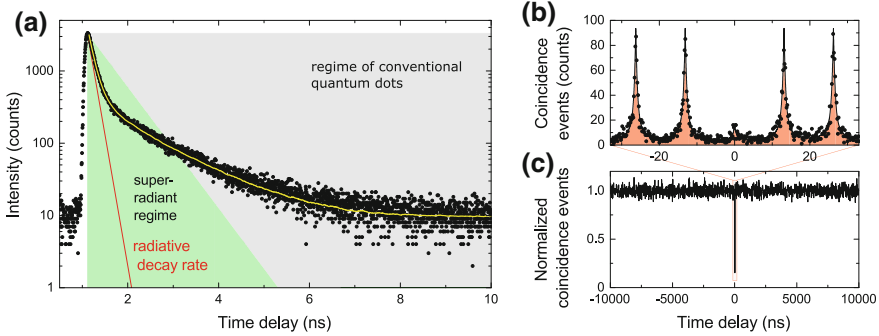


Fig. 5.17 Experimental demonstration of single-photon superradiance from a QD. **a** Time-resolved decay (*black points*) of the 1s exciton obtained under 2s-resonant excitation. The fit to the theoretical model is indicated by the *yellow line*. We take into account the impact of nonradiative processes presented in the previous section and extract a radiative decay rate of 8.4 ns^{-1} (*red line*), which is deeply in the superradiant regime (*green area*). **b** HBT measurement of the emitted photons showing $g^{(2)}(0) = 0.13$, which demonstrates the single-photon character of the emission. **c** Long-time-scale HBT measurement where each coincidence peak has been numerically integrated. No blinking of the emission is observed. Figure reproduced from [23]

We have measured the oscillator strength of 9 different QDs and found them all to be superradiant with an average oscillator strength of $f = 76 \pm 11$ [23]. Remarkably, an oscillator strength up to $f = 96 \pm 2$ is observed corresponding to an intrinsic radiative rate beyond 10 GHz. Such a highly superradiant QD can deliver a radiative flux of single photons equivalent to more than five conventional QDs.

While the microscopic structure of the out-of-plane wavefunction can be accurately computed because the quantum-well thickness is known with monolayer precision, the in-plane geometry is generally unknown. The information is then inferred from the superradiant enhancement S via (cf. Sect. 5.3.1)

$$L = \frac{a_{\text{QW}}}{\sqrt{2}} \frac{\sqrt{S}}{|\langle \phi_h | \phi_e \rangle|}. \quad (5.63)$$

From the measured value $S \simeq 4.3$ an in-plane diameter $2L \simeq 24 \text{ nm}$ is obtained. The exciton wavefunction is spread over 90 thousand atoms in a collective superradiant quantum state sharing a single excitation.

5.3.4 Impact of Thermal Effects on Single-Photon Superradiance

The quantization energy ΔE_{QD} scales inversely proportional to the QD size squared, $\Delta E_{\text{QD}} \propto L^{-2}$, and, thus, decreases dramatically for large QDs. If ΔE_{QD} is

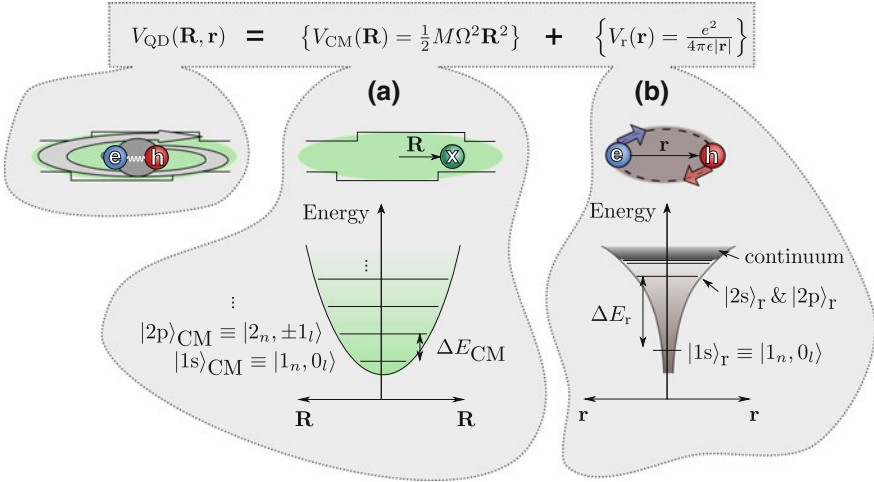


Fig. 5.18 Decomposition of the in-plane exciton dynamics into **a** a center-of-mass and **b** a relative motion. **a** The former describes the motion of the exciton center of mass in a two-dimensional harmonic potential, cf. (5.64). **b** The electron-hole electrostatic attraction is captured by the relative motion. Figure reproduced from [23]

comparable to the thermal energy, $k_B T$, excited states of the exciton manifold become populated and the large $1s$ oscillator strength is redistributed thus decreasing light-matter interaction. In the following we show that the temperature limits the maximum oscillator strength that can be harvested. In particular, the temperature of the current experiment of 7 K leads to a maximum oscillator strength of ~ 100 .

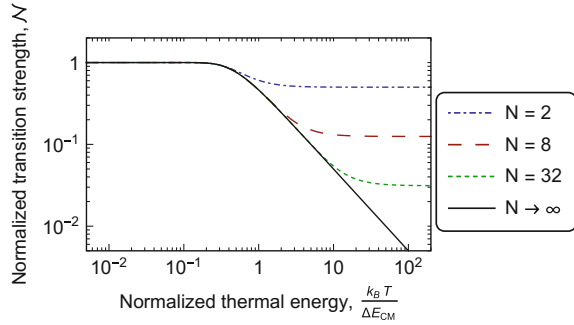
Since the exciton dynamics can be decomposed into a center-of-mass (CM) and a relative (r) motion, cf. (5.57) and (5.58), the ground state is denoted as $|1s\rangle_{\text{CM}}|1s\rangle_r$. The relative motion is equivalent to the two-dimensional Hydrogen problem [29, 74] and is governed by the mutual electron-hole attraction, see Fig. 5.18. In this subspace, the relevant energy difference ΔE_r between the ground $|1s\rangle_r$ and first excited $|2s\rangle_r$ states equals roughly twice the excitonic Rydberg energy and amounts to about 8 meV. At cryogenic temperatures, thermal energies are much smaller (below 1 meV) and thermal population of the relative-motion subspace can be neglected.

The center-of-mass motion is described by a particle in a two-dimensional harmonic potential $V_{\text{CM}}(\mathbf{R}) = (1/2)M\Omega^2\mathbf{R}^2$, cf. Fig. 5.18a, where M is the exciton mass and the spring constant Ω is related to the quantum-dot size L via [25] $\Omega = 4\hbar/ML^2$. The resulting energy eigenstates are given by [29]

$$E_{nl} = (2n - |l| - 1)\hbar\Omega, \tag{5.64}$$

where $n = 1, 2, 3, \dots$ and $l = 0, \pm 1, \dots, \pm(n - 1)$. The dipole selection rules dictate that states with $l = 0$ are bright (superradiant) and all others are dark (subradiant). For thermal energies $k_B T$ comparable to $\Delta E_{\text{CM}} = \hbar\Omega$, the excited states

Fig. 5.19 The normalized transition strength \mathcal{N} versus normalized thermal energy $k_B T / \hbar \Omega$ for different numbers of bound states N in a monolayer-fluctuation QD. Figure reproduced from [23]



become populated and the relevant figure of merit for light-matter interaction is the transition strength $F(T) = \mathcal{N}(T) \times f$, which is related to the oscillator strength via a temperature-dependent factor $\mathcal{N}(T)$. The latter describes the distribution of the population within the center-of-mass subspace. For a single excited state, $|e\rangle$, \mathcal{N} is given by

$$\mathcal{N}(T) = \frac{1 + \frac{f_e}{f} \mathcal{B}(T)}{1 + \mathcal{B}(T)}, \quad (5.65)$$

where $\mathcal{B}(T) = \exp(-\Delta E_{CM}/k_B T)$ is the Boltzmann factor and f_e is the oscillator strength of the excited state. If $|e\rangle$ is dark and the temperature is high, the transition strength is half of f ($\mathcal{N} = 1/2$). We generalize (5.65) with the help of (5.64) for an arbitrarily large subspace

$$\mathcal{N}(T) = \frac{\text{radiative contributions}}{\text{all contributions}} = \frac{\sum_{n=1}^N \mathcal{B}^{2(n-1)}}{\sum_{n=1}^N \sum_{l=-(n-1)}^{n-1} \mathcal{B}^{2(n-1)-|l|}}, \quad (5.66)$$

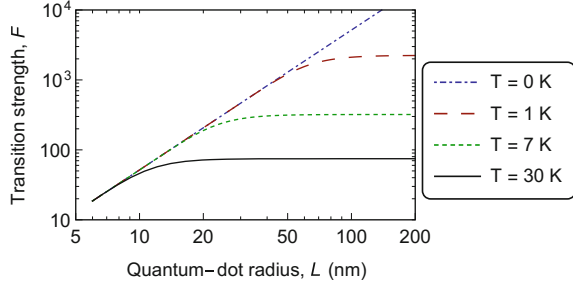
where N denotes the number of center-of-mass states. This expression can be evaluated analytically giving

$$\mathcal{N}(T) = \coth\left(\frac{\hbar \Omega}{2k_B T} N\right) \tanh\left(\frac{\hbar \Omega}{2k_B T}\right), \quad (5.67)$$

and is plotted in Fig. 5.19. At small temperatures $4k_B T \lesssim \hbar \Omega$, excited states play a negligible role and $F = f$. This is the regime in which the oscillator strength can be reliably measured. We employ this criterion $\hbar \Omega = 4k_B T$ to estimate the maximum oscillator strength $f_{\text{th,max}}^{\text{sym}}$ that can be resolved at a temperature T and obtain (we consider the out-of-plane overlap $|\langle \psi_h | \psi_e \rangle|^2 \approx 1$ for simplicity)

$$f_{\text{max,th}}^{\text{sym}} = \frac{4\hbar E_P}{M\omega_0^2} \frac{1}{k_B T}, \quad (5.68)$$

Fig. 5.20 The transition strength F versus QD radius L at different temperatures. For small QDs, F increases quadratically with L due to superradiance but saturates at larger values due to thermally activated excited states. Figure reproduced from [23]



which leads to an oscillator strength of 170 at 7 K. We generalize this expression for a more realistic asymmetric QD with an aspect ratio of $1:\xi$ with $\xi \geq 1$ and find that the maximum oscillator strength is decreased by ξ . We therefore conclude that oscillator strengths larger than about 100 are unlikely to be resolved at the experimental conditions of the present work. Remarkably, oscillator strengths of 1500 are predicted in monolayer-fluctuation QDs with a radius of about 60 nm. Temperatures below 0.8 K would, however, be required to resolve this effect.

The oscillator strength scales with the QD area $S \propto L^2$ but the normalized transition strength \mathcal{N} scales as L^{-2} , cf. (5.67). Thermal effects therefore saturate the transition strength F , which can be expressed using (5.62)

$$F = f_{\max} \left(\frac{\sqrt{2}L}{a_{\text{QW}}} \right)^2 \tanh \left(\frac{2\hbar^2}{Mk_{\text{B}}TL^2} \right), \quad (5.69)$$

which is plotted in Fig. 5.20. The transition strength saturates at

$$\lim_{L \rightarrow \infty} F = \frac{8\hbar E_p}{M\omega a_0^2} \frac{1}{k_{\text{B}}T}, \quad (5.70)$$

which is independent of L and, interestingly, happens to equal $2f_{\max, \text{th}}^{\text{sym}}$. Note that for very large $L \gtrsim 100$ nm, deviations from the electric-dipole approximation, which are not accounted for in this study, further reduce the transition strength [25].

5.4 Conclusion and Outlook

In this chapter we discussed two mesoscopic properties of QDs: the breakdown of the dipole theory and single-photon superradiance. Aside from the dipole moment, In(Ga)As QDs have a large mesoscopic moment that contains magnetic-dipole and electric-quadrupole contributions. The impact of the mesoscopic moment is especially pronounced in electromagnetic environments that are not parity symmetric. The developed microscopic theory shows that the mesoscopic moment originates

from distortions of the underlying crystal lattice. The resulting current density is curved leading to interaction of both electric and magnetic character. This opens the prospect for designing photonic nanostructures that match the shape of the QD current and thus enhance light-matter interaction efficiency. The simultaneous electric and magnetic nature of the QD current may lead to the vision of designing optical quantum metamaterials made from QDs for tailoring the interaction at the single-electron and single-photon level.

Single-photon superradiance was observed in monolayer-fluctuation QDs by recording the temporal decay dynamics in conjunction with second-order correlation measurements and a theoretical model. This enhanced light-matter coupling is known as the giant oscillator strength and was shown to be equivalent to superradiance. We argued that there is ample room for improving the oscillator strength at lower temperatures with prospects for generating highly coherent photons by out-speeding the noise sources, and for approaching the ultra-strong-coupling regime of cavity quantum electrodynamics with optical photons.

Acknowledgements We gratefully acknowledge the financial support from the Danish Council for Independent Research (natural sciences and technology and production sciences), the European Research Council (ERC consolidator grants “ALLQUANTUM” and “QIOS”), the Lundbeck Foundation and the Carlsberg Foundation.

References

1. P. Lodahl, S. Mahmoodian, S. Stobbe, *Rev. Mod. Phys.* **87**, 347 (2015)
2. J.P. Reithmaier, A. Löffler, C. Hofmann, S. Kuhn, S. Reitzenstein, L.V. Keldysh, V.D. Kulakovskii, T.L. Reinecke, A. Forchel, *Nature* **432**, 197 (2004)
3. E. Peter, P. Senellart, D. Martrou, A. Lemaître, J. Hours, J. Gérard, J. Bloch, *Phys. Rev. Lett.* **95**, 067401 (2005)
4. K. Hennessy, A. Badolato, M. Winger, D. Gerace, M. Atatüre, S. Gulde, S. Fält, E.L. Hu, A. Imamoglu, *Nature* **445**, 896 (2007)
5. G. Lecamp, P. Lalanne, J.P. Hugonin, *Phys. Rev. Lett.* **99**, 023902 (2007)
6. T. Lund-Hansen, S. Stobbe, B. Julsgaard, H. Thyrestrup, T. Sünnner, M. Kamp, A. Forchel, P. Lodahl, *Phys. Rev. Lett.* **101**, 113903 (2008)
7. J. Claudon, J. Bleuse, N.S. Malik, M. Bazin, P. Jaffrennou, N. Gregersen, C. Sauvan, P. Lalanne, J.-M. Gérard, *Nat. Photonics* **4**, 174 (2010)
8. A. Schwagmann, S. Kalliakos, I. Farrer, J.P. Griffiths, G.A.C. Jones, D.A. Ritchie, A.J. Shields, *Appl. Phys. Lett.* **99**, 261108 (2011)
9. A. Laucht, S. Pütz, T. Günthner, N. Hauke, R. Saive, S. Frédérick, M. Bichler, M.-C. Amann, A.W. Holleitner, M. Kaniber, J.J. Finley, *Phys. Rev. X* **2**, 011014 (2012)
10. M. Arcari, I. Söllner, A. Javadi, S. Lindskov Hansen, S. Mahmoodian, J. Liu, H. Thyrestrup, E.H. Lee, J.D. Song, S. Stobbe, P. Lodahl, *Phys. Rev. Lett.* **113**, 093603 (2014)
11. E.A. Muljarov, R. Zimmermann, *Phys. Rev. Lett.* **93**, 237401 (2004)
12. B. Urbaszek, E.J. McGhee, M. Krüger, R.J. Warburton, K. Karrai, T. Amand, B.D. Gerardot, P.M. Petroff, J.M. Garcia, *Phys. Rev. B* **69**, 035304 (2004)
13. I. Favero, A. Berthelot, G. Cassabois, C. Voisin, C. Delalande, P. Roussignol, R. Ferreira, J.M. Gérard, *Phys. Rev. B* **75**, 073308 (2007)
14. I. Wilson-Rae, A. Imamoglu, *Phys. Rev. B* **65**, 235311 (2002)

15. U. Hohenester, A. Laucht, M. Kaniber, N. Hauke, A. Neumann, A. Mohtashami, M. Seliger, M. Bichler, J.J. Finley, *Phys. Rev. B* **80**, 201311 (2009)
16. M. Calic, P. Gallo, M. Felici, K.A. Atlasov, B. Dwir, A. Rudra, G. Biasiol, L. Sorba, G. Tarel, V. Savona, E. Kapon, *Phys. Rev. Lett.* **106**, 227402 (2011)
17. K.H. Madsen, P. Kaer, A. Kreiner-Møller, S. Stobbe, A. Nysteen, J. Mørk, P. Lodahl, *Phys. Rev. B* **88**, 045316 (2013)
18. P. Kaer, P. Lodahl, A.-P. Jauho, J. Mork, *Phys. Rev. B* **87**, 081308 (2013)
19. E. Chekhovich, M. Makhonin, A. Tartakovskii, A. Yacoby, H. Bluhm, K. Nowack, L. Vandersypen, *Nat. Mater.* **12**, 494 (2013)
20. M.L. Andersen, S. Stobbe, A.S. Sørensen, P. Lodahl, *Nat. Phys.* **7**, 215 (2011)
21. P. Tighineanu, M.L. Andersen, A.S. Sørensen, S. Stobbe, P. Lodahl, *Phys. Rev. Lett.* **113**, 043601 (2014)
22. P. Tighineanu, A.S. Sørensen, S. Stobbe, P. Lodahl, *Phys. Rev. Lett.* **114**, 247401 (2015)
23. P. Tighineanu, R.S. Daveau, T.B. Lehmann, H.E. Beere, D.A. Ritchie, P. Lodahl, S. Stobbe, *Phys. Rev. Lett.* **116**, 163604 (2016)
24. D. Bruls, J. Vugs, P. Koenraad, H. Saleminck, J. Wolter, M. Hopkinson, M. Skolnick, F. Long, S. Gill, *Appl. Phys. Lett.* **81**, 1708 (2002)
25. S. Stobbe, P.T. Kristensen, J.E. Mortensen, J.M. Hvam, J. Mørk, P. Lodahl, *Phys. Rev. B* **86**, 085304 (2012)
26. J.R. Zurita-Sánchez, L. Novotny, *JOSA B* **19**, 1355 (2002)
27. J.R. Zurita-Sánchez, L. Novotny, *JOSA B* **19**, 2722 (2002)
28. S.V. Goupalov, *Phys. Rev. B* **68**, 125311 (2003)
29. M. Sugawara, *Phys. Rev. B* **51**, 10743 (1995)
30. A. Thränhardt, C. Ell, G. Khitrova, H.M. Gibbs, *Phys. Rev. B* **65**, 035327 (2002)
31. K. Jun Ahn, A. Knorr, *Phys. Rev. B* **68**, 161307 (2003)
32. P.T. Kristensen, J.E. Mortensen, P. Lodahl, S. Stobbe, *Phys. Rev. B* **88**, 205308 (2013)
33. M. Cotrufo, A. Fiore, *Phys. Rev. B* **92**, 125302 (2015)
34. E. Rashba, G. Gurgenishvili, *Sov. Phys. Solid State* **4**, 759 (1962)
35. J. Hours, P. Senellart, E. Peter, A. Cavanna, J. Bloch, *Phys. Rev. B* **71**, 161306 (2005)
36. L.C. Andreani, G. Panzarini, J.-M. Gérard, *Phys. Rev. B* **60**, 13276 (1999)
37. J. Guest, T. Stievater, X. Li, J. Cheng, D. Steel, D. Gammon, D. Katzer, D. Park, C. Ell, A. Thränhardt, G. Khitrova, H.M. Gibbs, *Phys. Rev. B* **65**, 241310 (2002)
38. D. Gammon, E. Snow, B. Shanabrook, D. Katzer, D. Park, *Phys. Rev. Lett.* **76**, 3005 (1996)
39. R. Dicke, *Phys. Rev.* **93**, 99 (1954)
40. D.A.B. Miller, *Quantum Mechanics for Scientists and Engineers* (Cambridge University Press, Cambridge, 2007)
41. P. Harrison, *Quantum Wells, Wires and Dots: Theoretical and Computational Physics of Semiconductor Nanostructures* (Wiley, New York, 2005)
42. P. Tighineanu, R. Daveau, E.H. Lee, J.D. Song, S. Stobbe, P. Lodahl, *Phys. Rev. B* **88**, 155320 (2013)
43. J. Dreiser, M. Atatüre, C. Galland, T. Müller, A. Badolato, A. Imamoglu, *Phys. Rev. B* **77**, 075317 (2008)
44. O. Stier, M. Grundmann, D. Bimberg, *Phys. Rev. B* **59**, 5688 (1999)
45. K. Sivalertporn, L. Mouchliadis, A.L. Ivanov, R. Philp, E.A. Muljarov, *Phys. Rev. B* **85**, 045207 (2012)
46. S. Schmitt-Rink, D.A.B. Miller, D.S. Chemla, *Phys. Rev. B* **35**, 8113 (1987)
47. G. Bester, S. Nair, A. Zunger, *Phys. Rev. B* **67**, 161306 (2003)
48. M. Bayer, G. Ortner, O. Stern, A. Kuther, A.A. Gorbunov, A. Forchel, P. Hawrylak, S. Fafard, K. Hinzer, T.L. Reinecke, S.N. Walck, J.P. Reithmaier, F. Klopff, F. Schäfer, *Phys. Rev. B* **65**, 195315 (2002)
49. D.P. Craig, T. Thirunamachandran, *Molecular Quantum Electrodynamics: An Introduction to Radiation-Molecule Interactions* (Courier Dover Publications, New York, 1998)
50. P. Tighineanu, Electric and Magnetic Interaction Between Quantum Dots and Light. Ph.D. thesis, The Niels Bohr Institute, Faculty of Science, University of Copenhagen (2015)

51. N. Vats, S. John, K. Busch, *Phys. Rev. A* **65**, 043808 (2002)
52. L. Novotny, B. Hecht, *Principles of Nano-Optics* (Cambridge University Press, Cambridge, 2012)
53. J. Johansen, S. Stobbe, I.S. Nikolaev, T. Lund-Hansen, P.T. Kristensen, J.M. Hvam, W.L. Vos, P. Lodahl, *Phys. Rev. B* **77**, 073303 (2008)
54. D. Englund, A. Faraon, I. Fushman, N. Stoltz, P. Petroff, J. Vučković, *Nature* **450**, 857 (2007)
55. N. Somaschi, V. Giesz, L. De Santis, J. Loredano, M. Almeida, G. Hornecker, S. Portalupi, T. Grange, C. Antón, J. Demory, C. Gómez, I. Sagnes, N. Lanzillotti-Kimura, A. Lemaitre, A. Auffeves, A. White, L. Lanco, P. Senellart, *Nat. Photonics* **10**, 340 (2016)
56. A.G. Curto, T.H. Taminiau, G. Volpe, M.P. Kreuzer, R. Quidant, N.F. van Hulst, *Nat. Commun.* **4**, 1750 (2013)
57. P. Yao, V. Manga Rao, S. Hughes, *Laser Photonics Rev.* **4**, 499 (2010)
58. S. Stobbe, J. Johansen, P.T. Kristensen, J.M. Hvam, P. Lodahl, *Phys. Rev. B* **80**, 155307 (2009)
59. J. Johansen, B. Julsgaard, S. Stobbe, J.M. Hvam, P. Lodahl, *Phys. Rev. B* **81**, 081304 (2010)
60. S. DeBeer George, T. Petrenko, F. Neese, *Inorganica Chimica Acta* **361**, 965 (2008)
61. S. Bernadotte, A.J. Atkins, C.R. Jacob, *J. Chem. Phys.* **137**, 204106 (2012)
62. H. Eisele, A. Lenz, R. Heitz, R. Timm, M. Dähne, Y. Temko, T. Suzuki, K. Jacobi, *J. Appl. Phys.* **104**, 124301 (2008)
63. M. Noecker, B. Masterson, C. Wieman, *Phys. Rev. Lett.* **61**, 310 (1988)
64. I.D. Rukhlenko, D. Handapangoda, M. Premaratne, A.V. Fedorov, A.V. Baranov, C. Jagadish, *Opt. Express* **17**, 17570 (2009)
65. T.H. Taminiau, S. Karaveli, N.F. van Hulst, R. Zia, *Nat. Commun.* **3**, 979 (2012)
66. G.Y. Slepyan, A. Magyarov, S.A. Maksimenko, A. Hoffmann, *Phys. Rev. B* **76**, 195328 (2007)
67. J. Kalkman, H. Gersen, L. Kuipers, A. Polman, *Phys. Rev. B* **73**, 075317 (2006)
68. D.E. Chang, A.S. Sørensen, P.R. Hemmer, M.D. Lukin, *Phys. Rev. B* **76**, 035420 (2007)
69. L.D. Landau, E.M. Lifšic, J.B. Sykes, J.S. Bell, M. Kearsley, L.P. Pitaevskii, *Electrodynamics of Continuous Media* (Pergamon Press, Oxford, 1960)
70. E. Hanamura, *Phys. Rev. B* **37**, 1273 (1988)
71. E. Poem, Y. Kodriano, C. Tradonsky, N.H. Lindner, B.D. Gerardot, P.M. Petroff, D. Gershoni, *Nat. Phys.* **6**, 993 (2010)
72. C. Gerry, P. Knight, *Introductory Quantum Optics* (Cambridge University Press, Cambridge, 2005)
73. M. Davanço, C.S. Hellberg, S. Ates, A. Badolato, K. Srinivasan, *Phys. Rev. B* **89**, 161303 (2014)
74. W. Que, *Phys. Rev. B* **45**, 11036 (1992)